SUPPORTING INFORMATION

Dominant Role of Entropy in Stabilizing Sugar Isomerization Transition States within Hydrophobic Zeolite Pores

Michael J. Cordon[1], James W. Harris[1], Juan Carlos Vega-Vila[1], Jason S. Bates[1], Sukhdeep Kaur[2], Mohit Gupta[2], Megan E. Witzke[3], Evan C. Wegener[1], Jeffrey T. Miller[1], David W. Flaherty[3], David D. Hibbitts[2], Rajamani Gounder[1,*]

[1]*Charles D. Davidson School of Chemical Engineering, Purdue University, 480 Stadium Mall Drive, West Lafayette, IN 47907, USA*

[2]*Department of Chemical Engineering, University of Florida, 1030 Center Drive, Gainesville, FL 32611, USA*

[3]*Department of Chemical and Biomolecular Engineering, University of Illinois Urbana-Champaign, Urbana, IL 61801, United States*

*Corresponding author. E-mail: rgounder@purdue.edu

Table of Contents

S.1. Bulk structural and Lewis acid site characterization of Ti-Beta zeolites

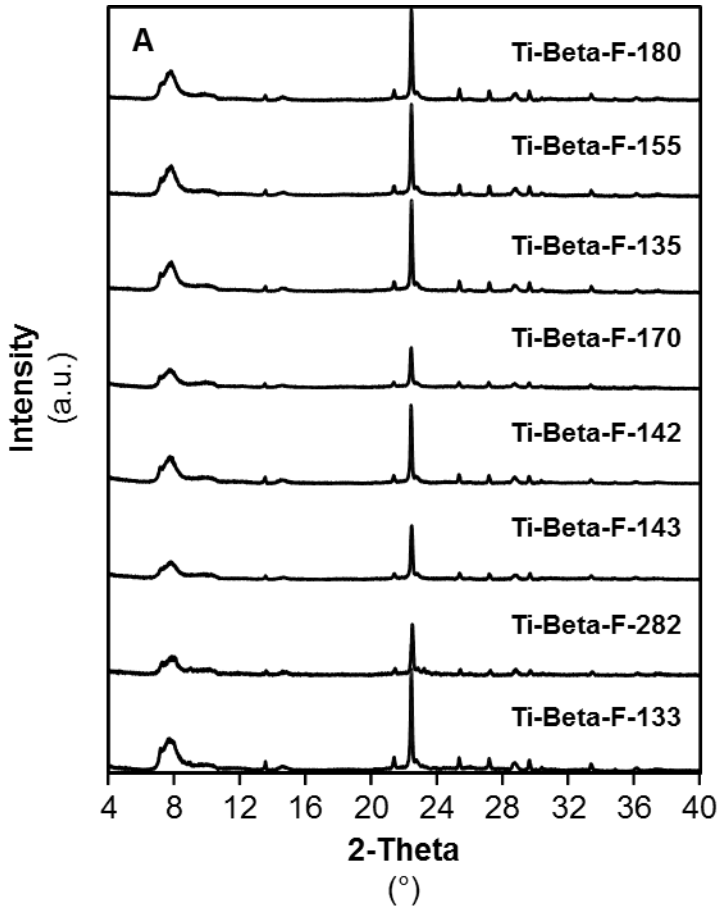

Figure S.1A. Powder XRD patterns of Ti-Beta-F samples studied in this work. Weak signals around 9-10° reflect an artifact from the sample holders used to collect XRD patterns.

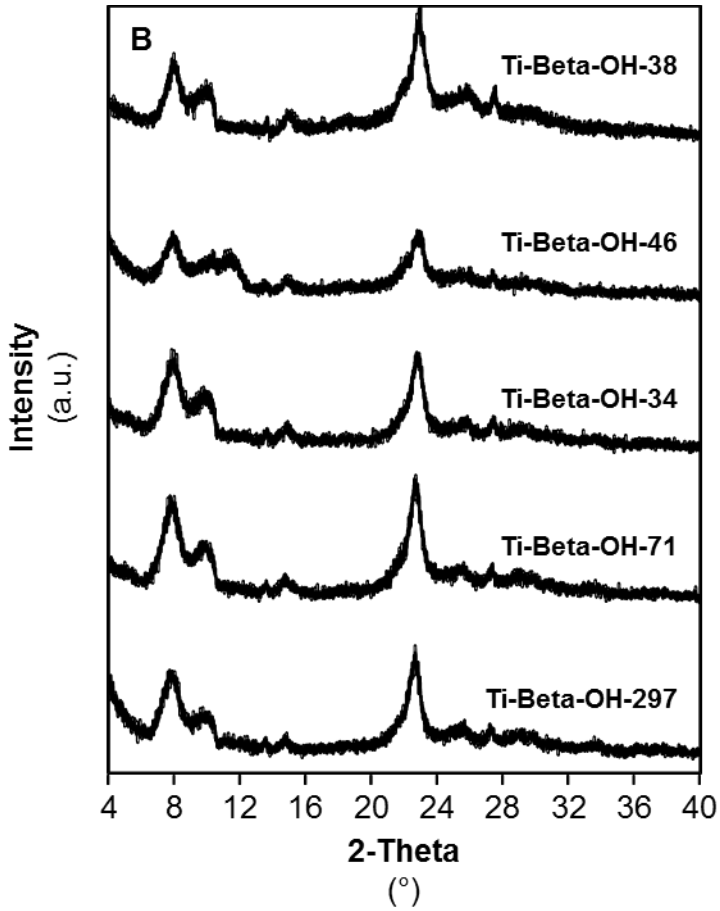

Figure S.1B. Powder XRD patterns of Ti-Beta-OH samples studied in this work. Weak signals around 9-10° reflect an artifact from the sample holders used to collect XRD patterns.

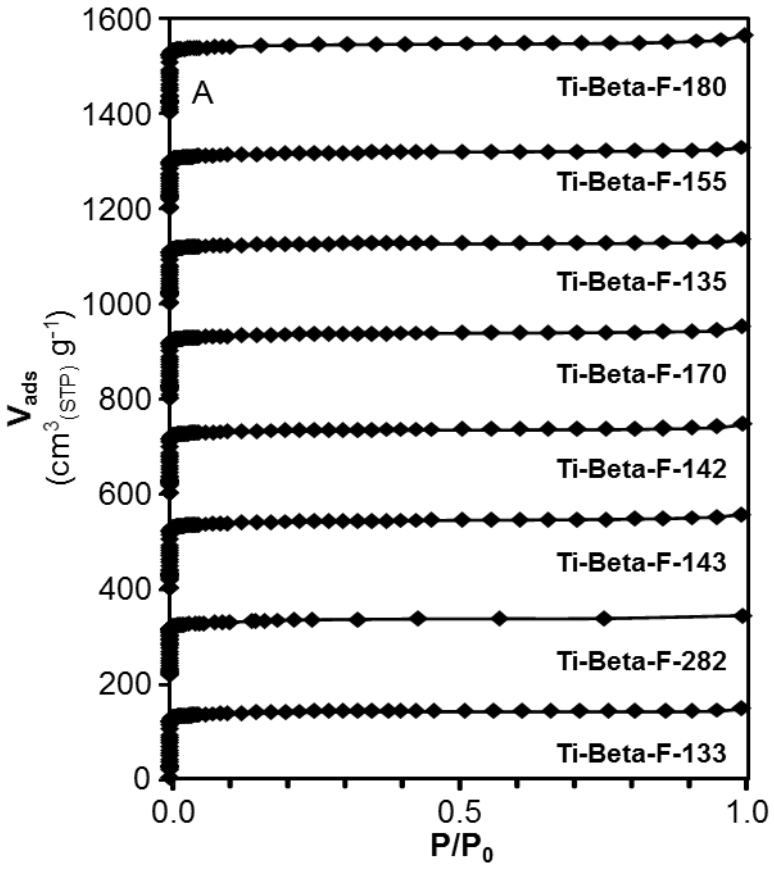

Figure S.2A. N_2 adsorption isotherms (77 K) of Ti-Beta-F samples studied in this work. Isotherms are offset by 200 cm^3 g^{-1} for clarity.

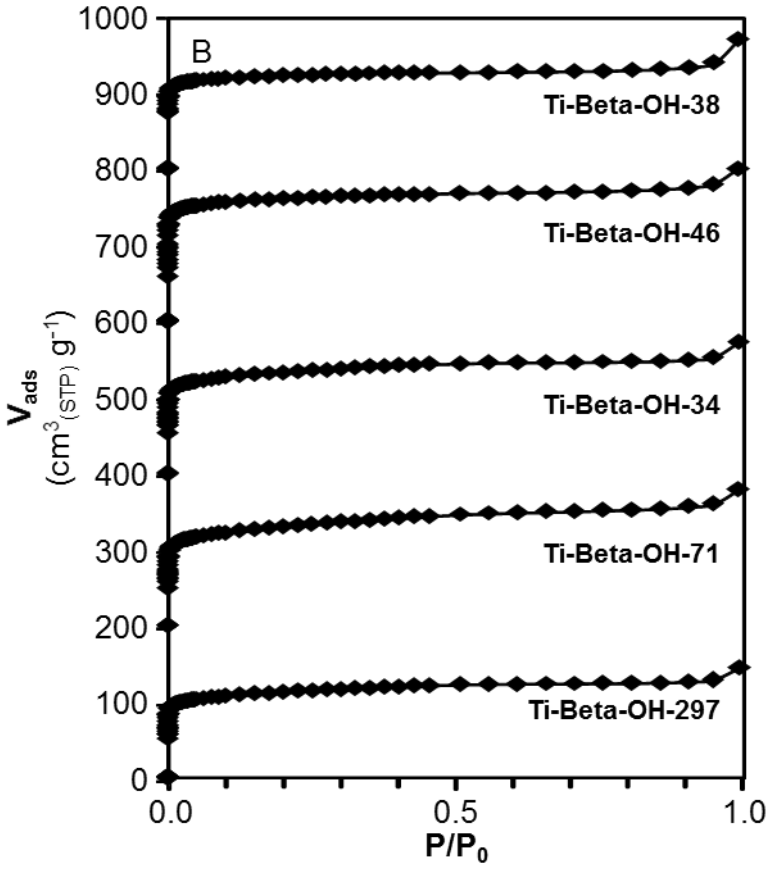

Figure S.2B. N_2 adsorption isotherms (77 K) of Ti-Beta-OH samples studied in this work. Isotherms are offset by 200 cm^3 g^{-1} for clarity.

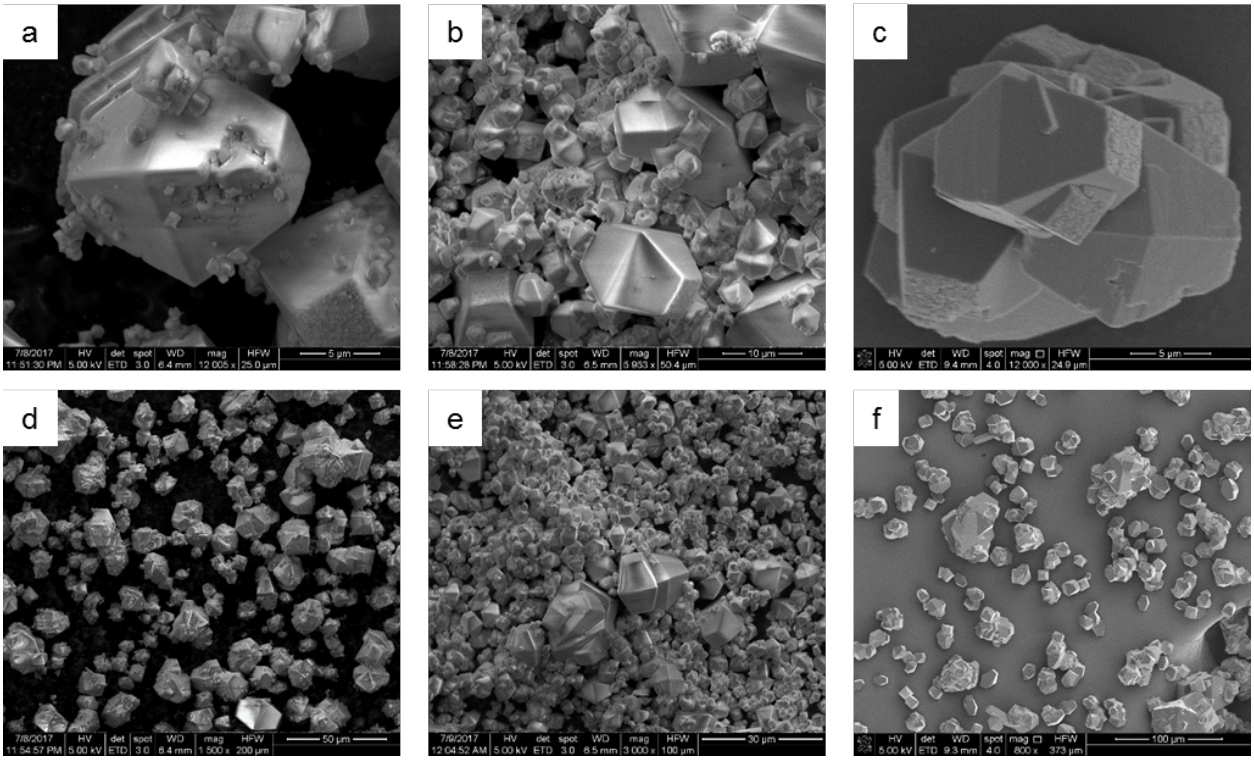

Figure S.3. SEM images of selected Ti-Beta-F samples: (a) Ti-Beta-F-135, (b) Ti-Beta-F-155, and (c) Ti-Beta-F-180. Bulk sample uniformity is assumed based on images for (d) Ti-Beta-F-135, (e) Ti-Beta-F-155, and (f) Ti-Beta-F-180. Larger crystal aggregates reflect Si-Beta-F seeds used to nucleate the formation of Ti-Beta-F.

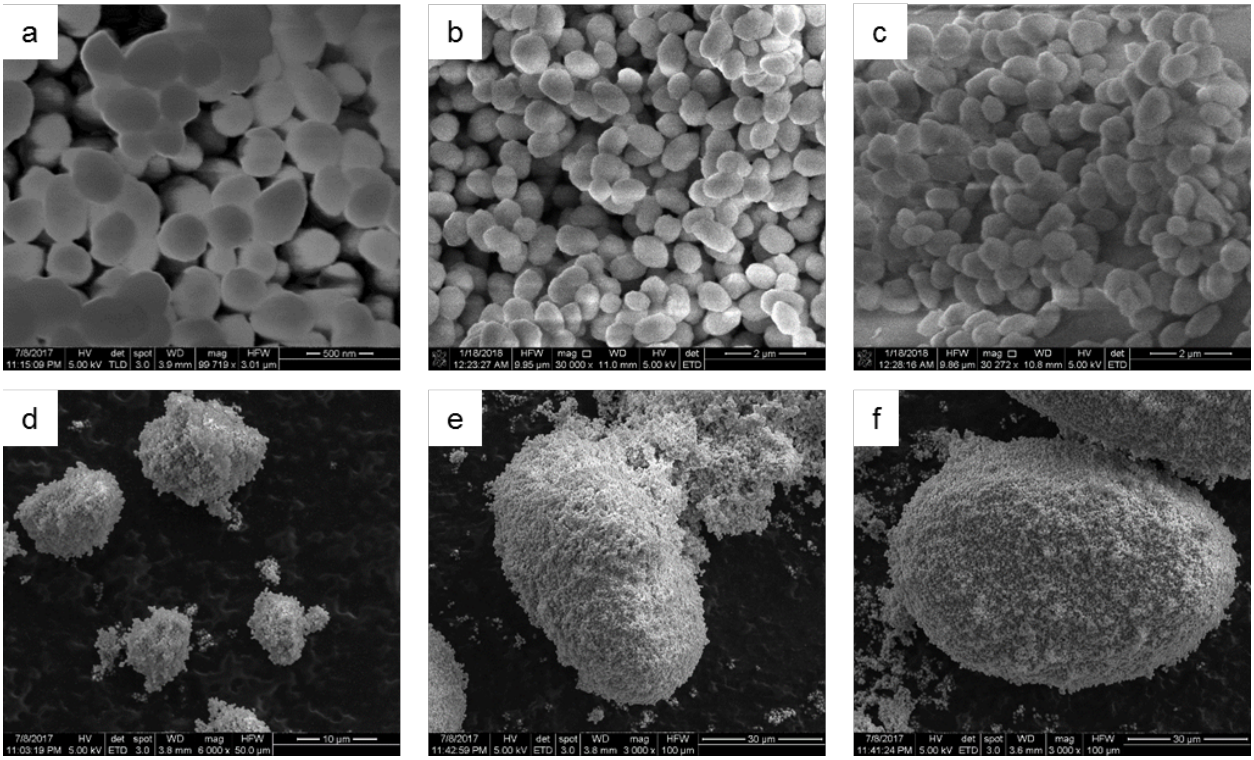

Figure S.4. SEM images of selected Ti-Beta-OH samples: (a) Ti-Beta-OH-46, (b) Ti-Beta-OH-34, and (c) Ti-Beta-OH-71. Bulk sample uniformity is assumed based on images for (d) Ti-Beta-OH-46, (e) Ti-Beta-OH-34, and (f) Ti-Beta-OH-71 which show larger agglomerates of small crystals.

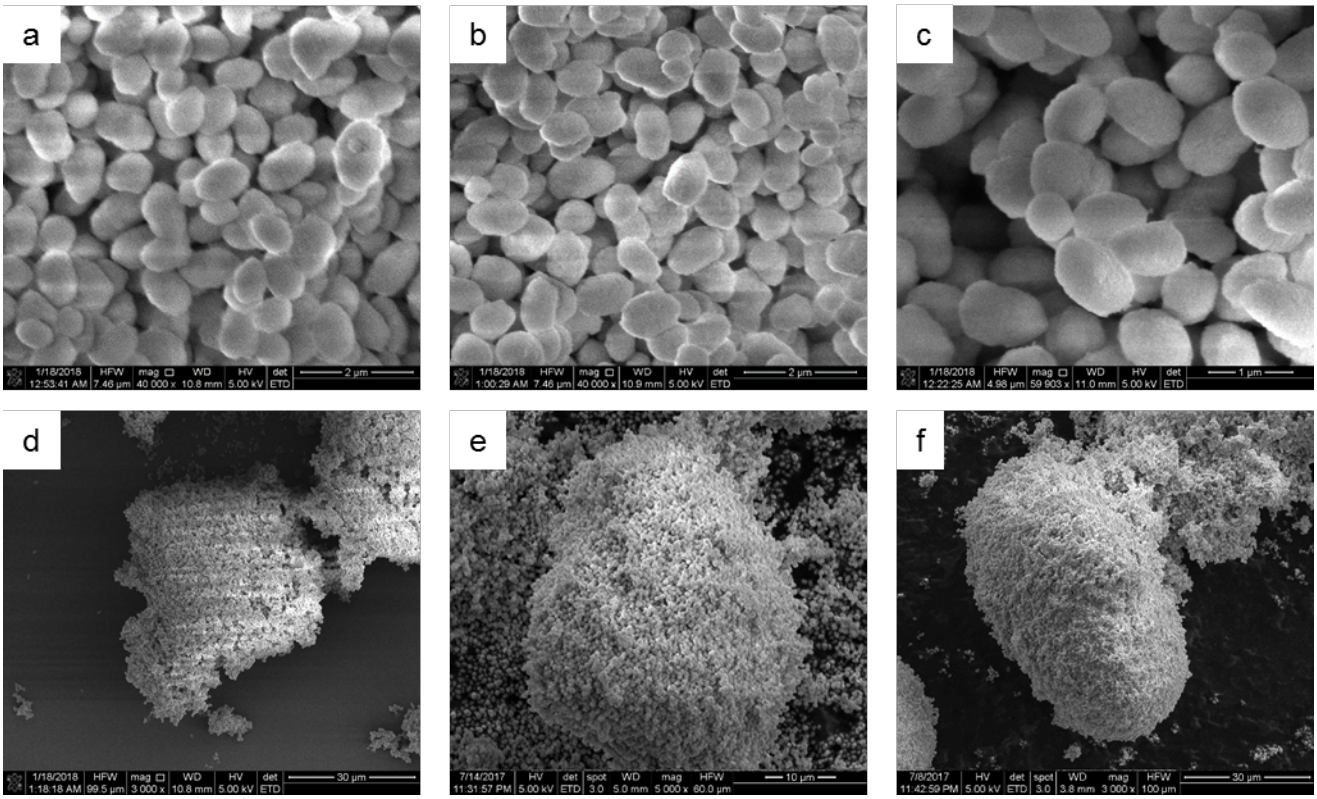

Figure S.5. SEM images of Ti-Beta-OH-34 at various steps of the synthesis procedure: (a) Al-Beta parent material, (b) after nitric acid treatment for dealumination, and (c) after $TiCl_4$ grafting to form Ti-Beta-OH-34. Bulk sample uniformity is assumed based on images for (d) Al-Beta parent material, (e) after nitric acid treatment for dealumination, and (f) after $TiCl_4$ grafting to form Ti-Beta-OH-34. All show larger agglomerates of small crystals.

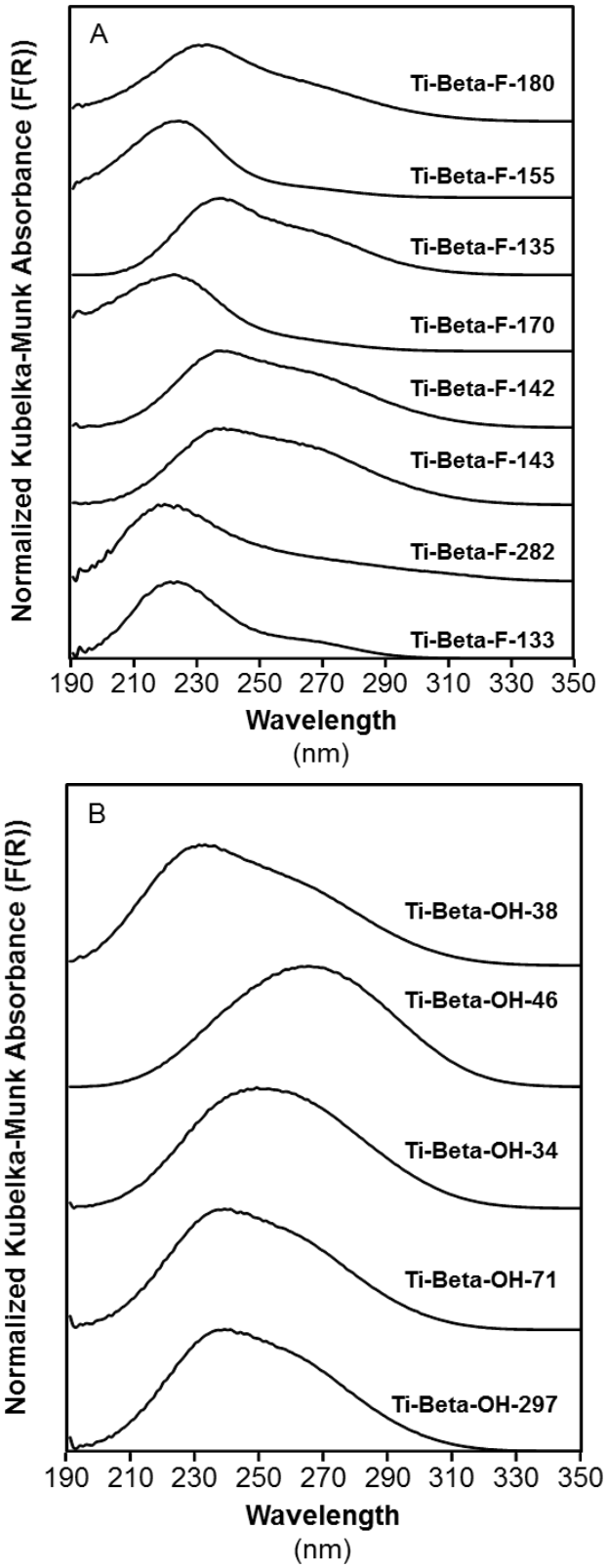

Figure S.6. Hydrated UV-Vis spectra of (A) Ti-Beta-F and (B) Ti-Beta-OH samples studied in this work collected prior to dehydration at 523 K.

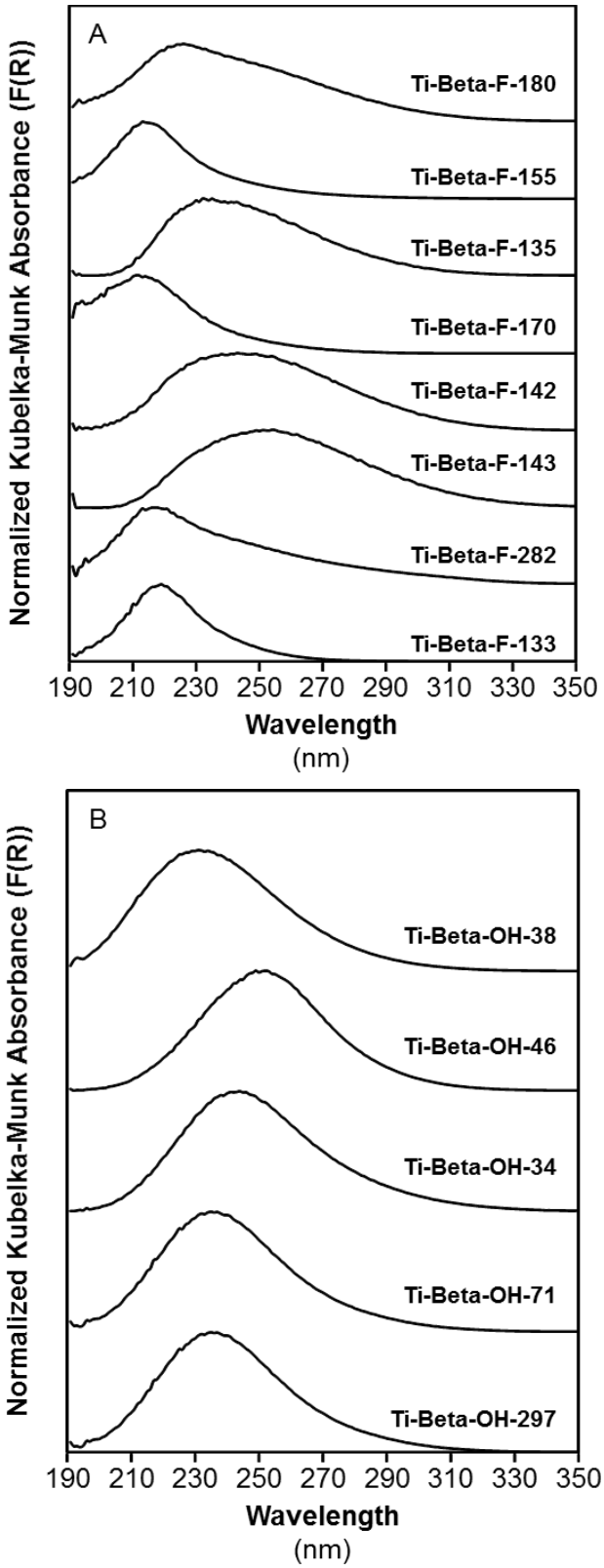

Figure S.7. Dehydrated UV-Vis spectra (523 K, 1800 s) of (A) Ti-Beta-F and (B) Ti-Beta-OH samples studied in this work.

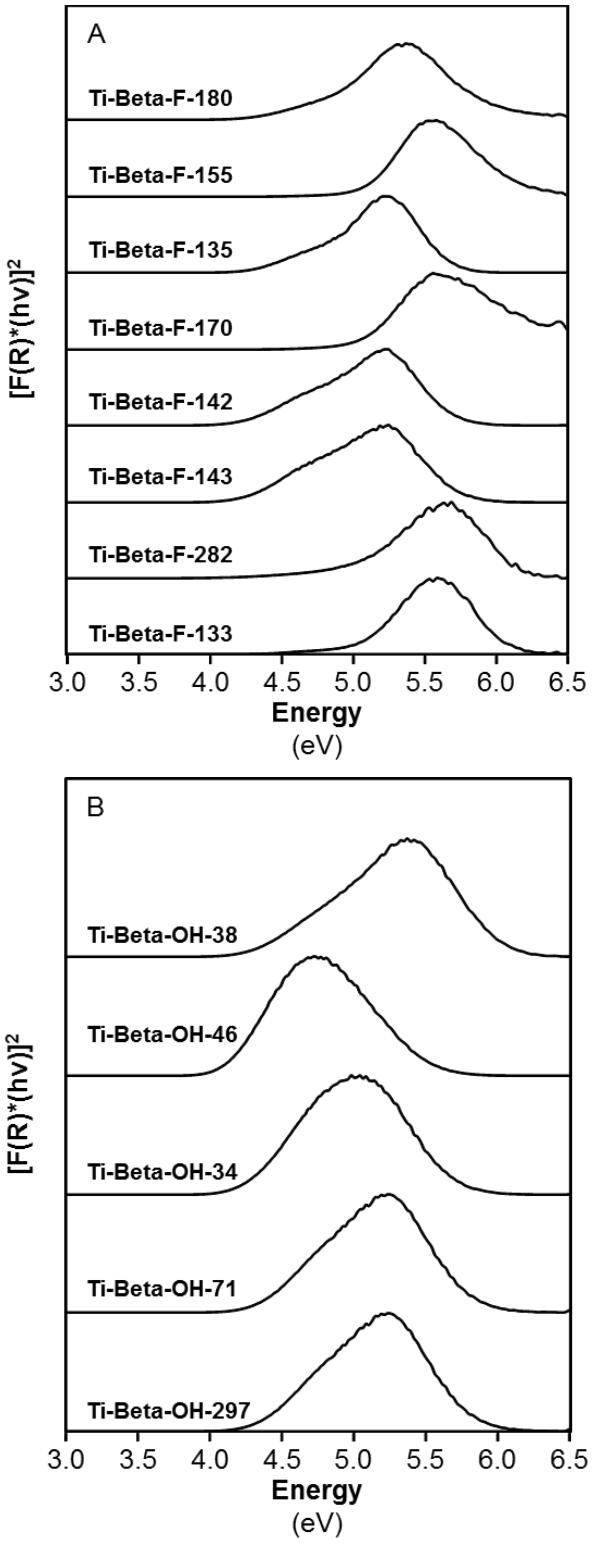

Figure S.8. Tauc plots of (A) Ti-Beta-F and (B) Ti-Beta-OH samples studied in this work prior to heating and sample dehydration ("hydrated" samples). Edge energies are summarized in Table S.1.

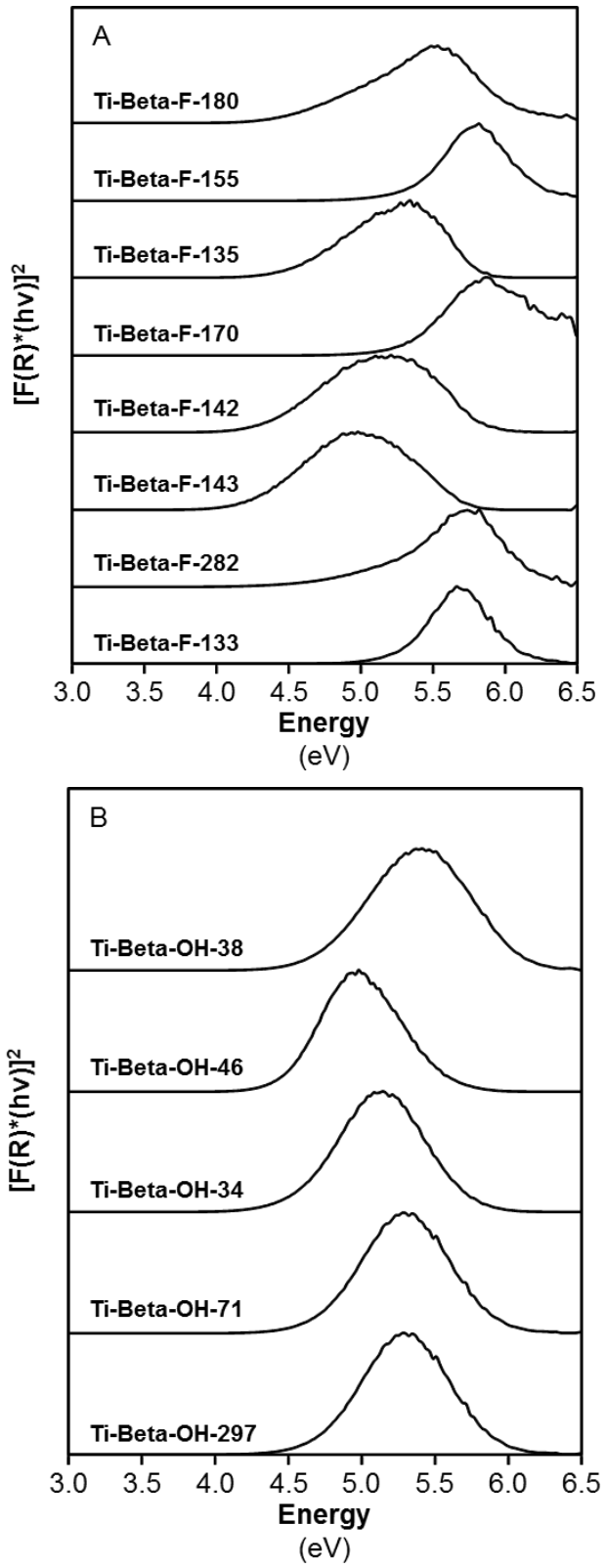

Figure S.9. Tauc plots of (A) Ti-Beta-F and (B) Ti-Beta-OH samples studied in this work after treatment in flowing He at 523 K for 1800 s. Edge energies are summarized in Table S.1.

Figures S.6 and S.7 above show UV-Vis spectra collected before and after the exposure of Ti-Beta samples to heat treatments (523 K, 1800 s). Band maxima do not shift significantly upon dehydration treatments. Tauc plots corresponding to these spectra are shown in Figures S.8 and S.9 and edge energies are x-intercept values measured from extrapolating the first linear regions at low energies of Tauc plots. Dehydration of each sample leads to an increase in the edge energy as shown in Table S.1. These shifts in edge energy upon dehydration corroborate the changes in Ti coordination number observed in XAS measurements detailed below (Section S.4.3).

Table S.1. Edge energies of Ti-Beta samples after exposure to ambient conditions, dehydrated, and rehydrated in wet Ar flow. Band maxima correspond to the primary UV-Vis F(R) peaks after dehydration shown in Figure S.6 above.

	Edge Energies			
Sample	**Ambient (eV)**	**Dehydrated (eV)**	**Rehydrated (eV)**	**Band Maximum (nm)**
Ti-Beta-F-180	4.4	4.4	4.3	230
Ti-Beta-F-155	5.1	5.3	5.1	216
Ti-Beta-F-135	4.3	4.5	4.3	231
Ti-Beta-F-170	5.1	5.3	5.1	216
Ti-Beta-F-142	4.2	4.3	4.3	246
Ti-Beta-F-143	4.2	4.2	4.2	253
Ti-Beta-F-282	5.0	5.1	5.0	218
Ti-Beta-F-133	5.1	5.3	5.0	219
Ti-Beta-OH-38	4.3	4.7	4.4	234
Ti-Beta-OH-46	4.1	4.4	4.1	253
Ti-Beta-OH-34	4.2	4.5	4.3	246
Ti-Beta-OH-71	4.3	4.7	4.4	235
Ti-Beta-OH-18	4.2	4.5	4.2	235

[a] Dehydration performed in dry flowing Ar to 523 K and held for 30 min.
[b] Rehydration performed in wet flowing Ar at ambient temperature.

S.1.1. IR characterization of titanosilicate samples using adsorbed CD_3CN

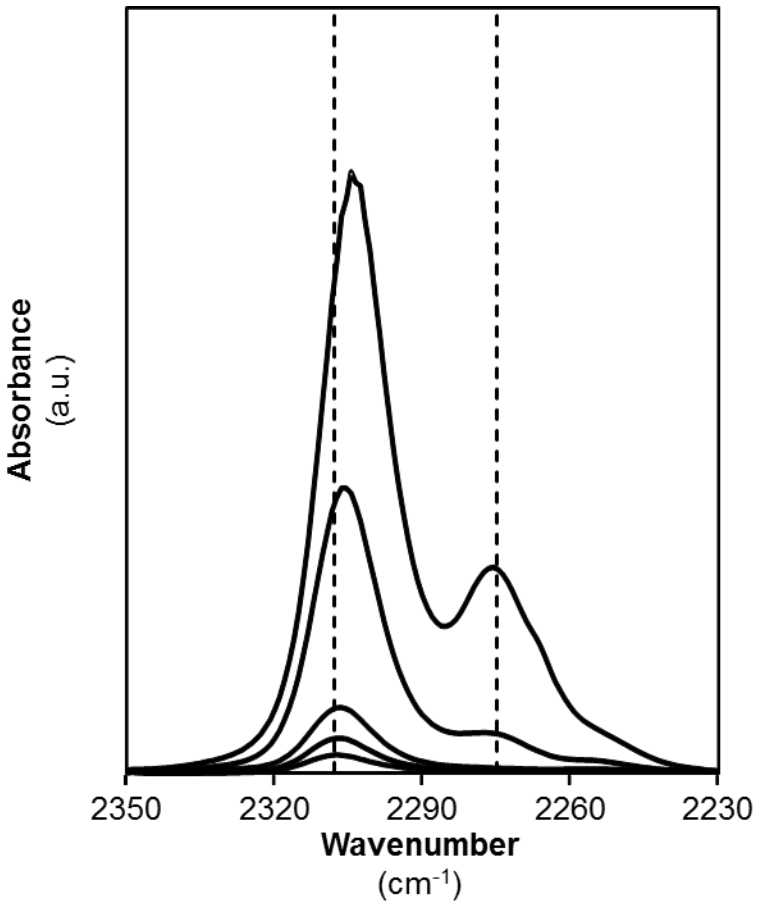

Figure S.10. IR spectra on Ti-Beta-OH-46 after progressive titration of CD_3CN at 303 K (CD_3CN/Ti = 0.002-2.34). Dashed lines are drawn at 2308 cm^{-1} (CD_3CN bound to Lewis acidic Ti) and 2275 cm^{-1} (CD_3CN hydrogen bound to silanols). Note that the peak center shifts slightly to lower wavenumbers with increasing adsorbed CD_3CN concentrations.

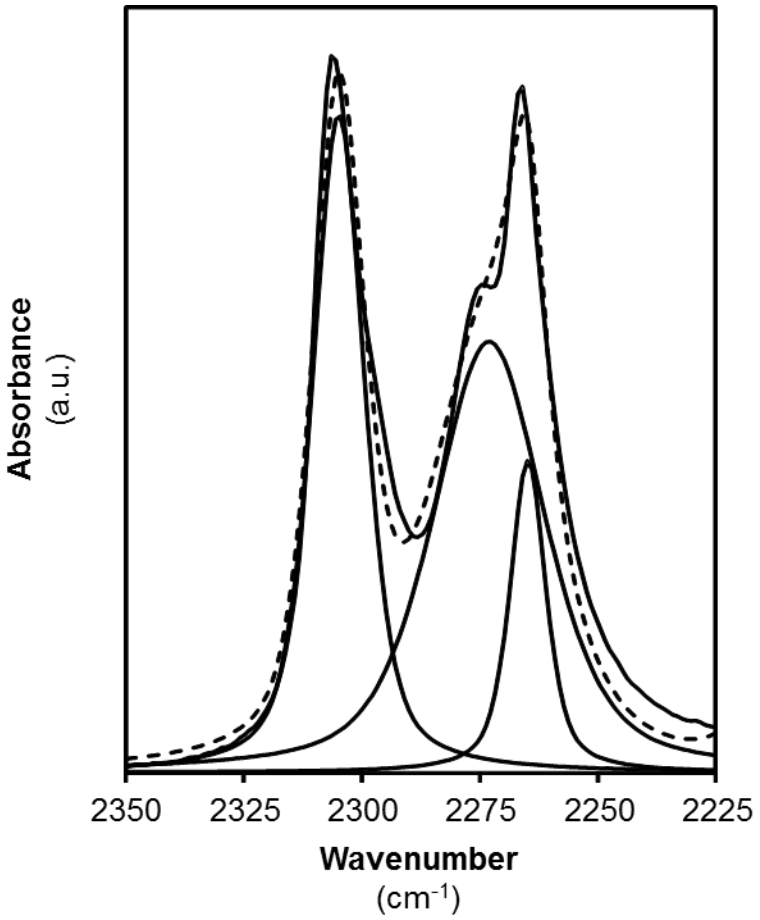

Figure S.11. CD_3CN-saturated IR spectra for Ti-Beta-F-155. The thickest solid line reflects the measured spectra upon saturation with CD_3CN while thinner lines indicate constitute peaks associated with CD_3CN bound to Lewis acidic Ti sites (2308 cm^{-1}), CD_3CN bound to silanols (2275 cm^{-1}), and gas phase physisorbed CD_3CN (2265 cm^{-1}). The dashed line represents the modeled spectra from combining deconvoluted peaks.

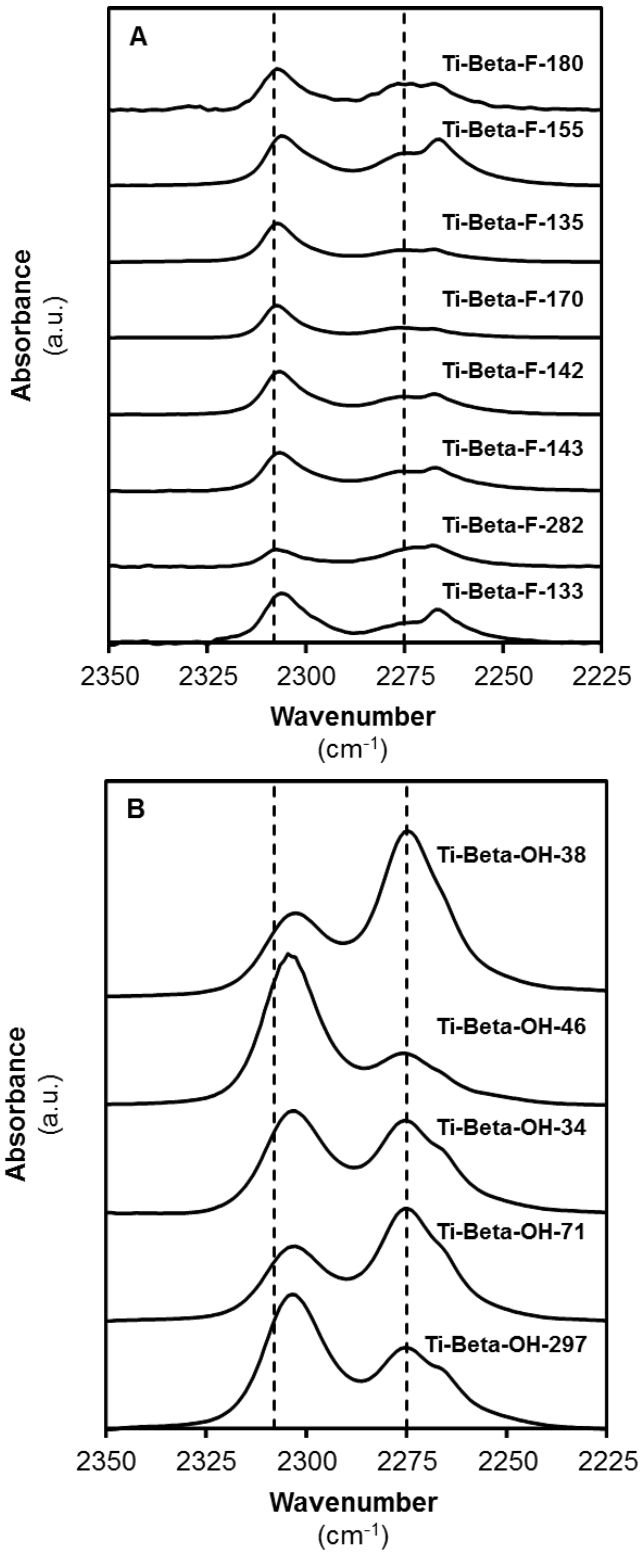

Figure S.12. IR spectra collected on (A) CD_3CN-saturated Ti-Beta-F and (B) CD_3CN-saturated Ti-Beta-OH samples studied in this work. Dashed lines are drawn at 2308 cm^{-1} (CD_3CN bound to Lewis acidic Ti) and 2275 cm^{-1} (CD_3CN bound to silanols).

S.1.2. IR characterization of titanosilicate samples using adsorbed pyridine

Pyridine (Alfa Aesar, >99%) adsorption on self-supporting Ti-Beta wafers was performed following similar procedures to those reported for CD_3CN titration at 423 K under static vacuum conditions including freeze-pump-thaw cycles, pyridine dosing and equilibration, dynamic vacuum exposure to remove residual gaseous titrant upon saturation, and baseline correction, normalization, and subtraction of parent spectra, resulting in IR spectra similar to those shown in Figure S.13A. Figure S.13A shows pyridine adsorption spectra with incremental pyridine doses on Ti-Beta-F-135. IR spectra on pyridine saturated Ti-Beta-F-155 is shown in Figure S.13B which can be deconvoluted to isolate the peak centered at 1605 cm^{-1}.

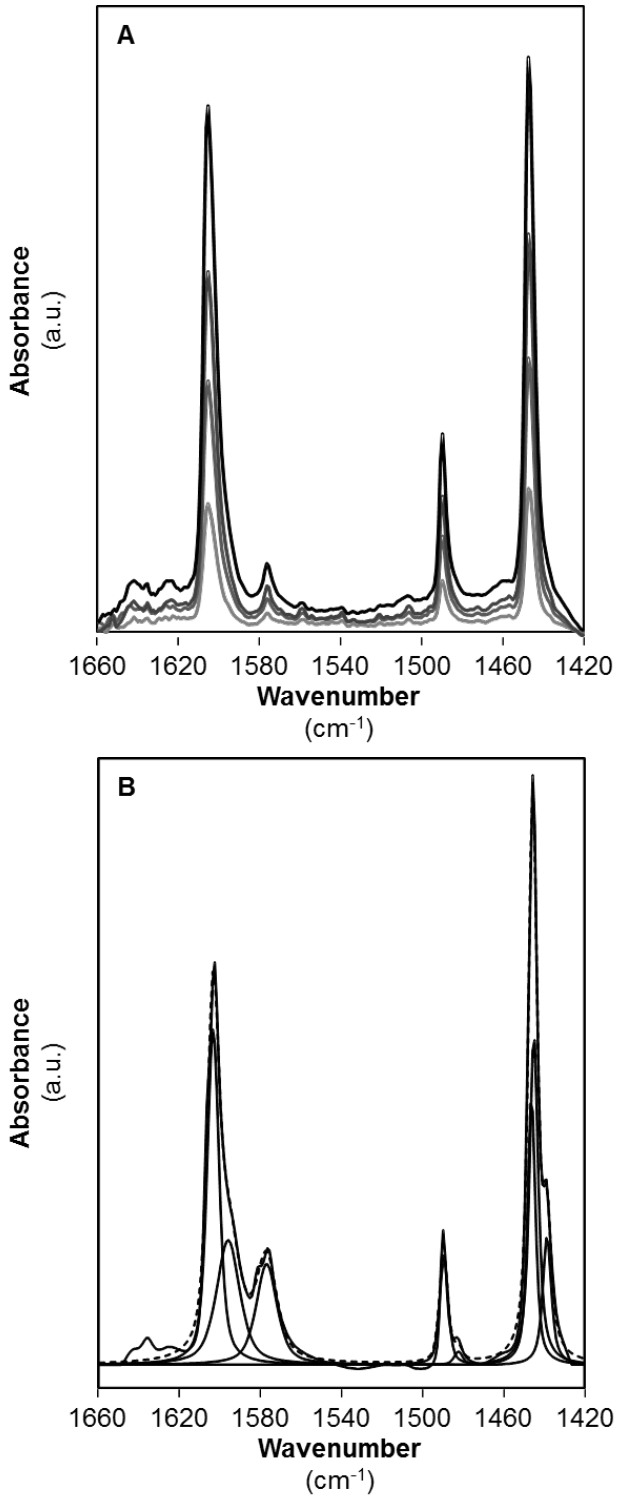

Figure S.13. IR spectra measured (a) after the first four doses of pyridine on Ti-Beta-F-135 (0.015-0.058 mol pyridine (mol Ti)$^{-1}$) and (b) after saturation of Ti-Beta-F-135 with pyridine (1.05 mol pyridine (mol Ti)$^{-1}$). The components included in the deconvolution are shown (thin solid lines) with the resulting fit envelope (dotted line) and the measured spectra (thick solid line).

Marginal increases in integrated area of the feature centered at 1605 cm^{-1} correlate linearly with marginal increases in adsorbed pyridine. The linear increase can be quantified on four distinct Ti-Beta samples which show similar molar extinction coefficients for pyridine adsorption from identical analyses to those of CD_3CN molar extinction coefficient determination in the main text, as seen in Figure S.14A and Table S.2. Averaging the linear increases in 1605 cm^{-1} peak area at low pyridine doses (Figure S.12B) yields a single $E(1605\ cm^{-1})$ value of 1.16 ± 0.23 cm μmol^{-1} which can then be used to quantify total Lewis acid density from IR spectra after pyridine saturation on each sample (Table 1, Main Text).

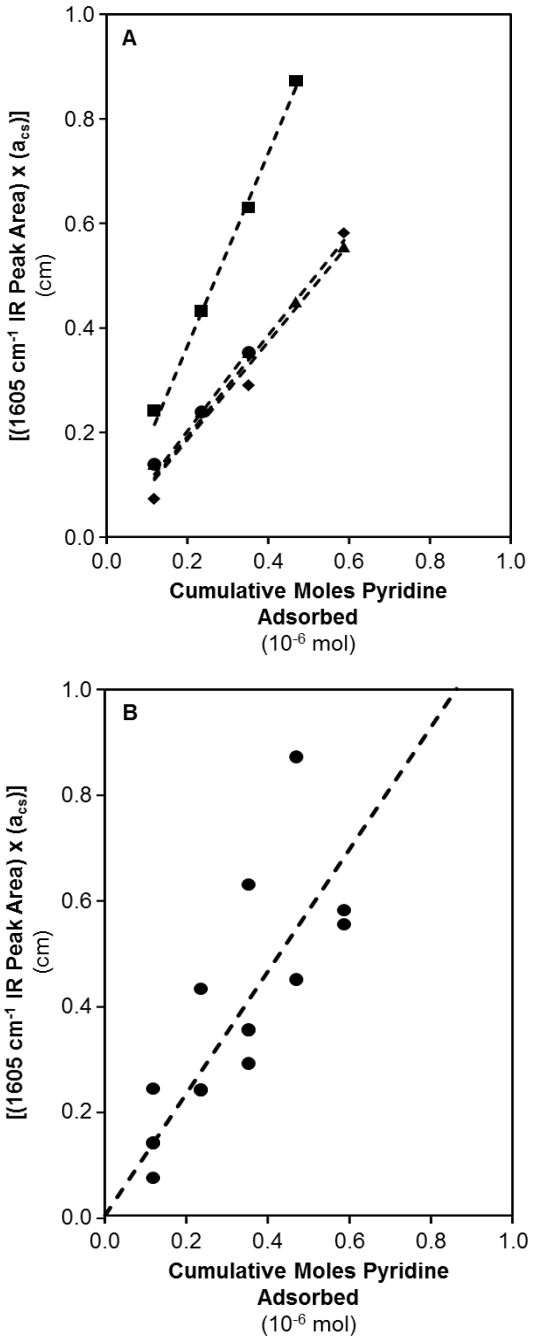

Figure S.14. (A) Integrated peak area normalized by wafer cross-sectional areas for the IR feature centered at 1605 cm^{-1} as a function of moles pyridine adsorbed onto Ti-Beta-F-155 (◆), Ti-Beta-F-135 (●), Ti-Beta-F-170 (▲), and Ti-Beta-OH-46 (■). Dashed lines indicate best fit lines through the origin for each sample with slopes equal to integrated molar extinction coefficients as listed in Table S.3. (B) Integrated peak area normalized by wafer cross-sectional areas for the IR feature centered at 1605 cm^{-1} as a function of moles pyridine adsorbed onto Ti-Beta-F-155, Ti-Beta-F-135, Ti-Beta-F-170, and Ti-Beta-OH-46 as a single data set (●). The dashed line indicates the best fit line through the origin for the combined data set with the slope equal to the average integrated molar extinction coefficient.

Table S.2. *E*(1605 cm^{-1}) values determined for four separate Ti-Beta samples by sequentially dosing pyridine at 423 K.

Sample	E(1605 cm^{-1}) (cm μmol^{-1})
Ti-Beta-F-135	1.84
Ti-Beta-F-170	0.97
Ti-Beta-OH-46	0.93
Ti-Beta-F-155	1.02

Figure S.15 shows Lewis acid site densities determined from pyridine-saturation infrared experiments plotted against Lewis acid site densities determined from CD_3CN-saturation infrared experiments from Table 2. The two sets of Lewis acid site concentrations linearly correlate with one another, suggesting that they reflect similar site densities.

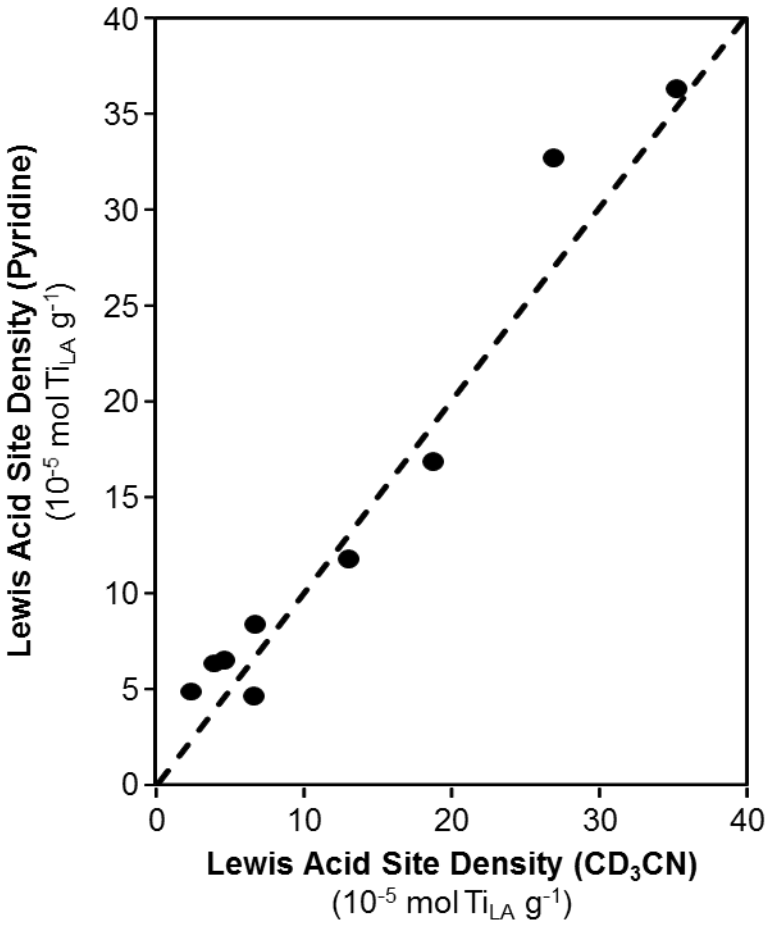

Figure S.15. Lewis acid site densities determined from pyridine-saturation IR experiments plotted against Lewis acid site densities determined from CD_3CN-saturation IR experiments. The dashed line is a parity line drawn to guide the eye.

S.1.3. Assessing extracrystalline surface areas and normalized silanol densities on titanosilicate samples

Ti-Beta-F crystals exhibit square bipyramidal crystal morphology (Figure S.3). Characteristic lengths were measured along the plane corresponding to the symmetric crystal center and along the terminal planes and the characteristic height was measured as the distance between those two planes. Characteristic length and height measurements were obtained from SEM images of more than 25 individual crystals selected randomly from multiple locations. Surface area and volume measurements were obtained by treating crystals as square frustums sharing a common base along a symmetrical middle plane.

For Ti-Beta-OH samples, the size of the final material is dependent on the size of the Al-Beta parent material which is maintained after dealumination and grafting as shown in Figure S.5. Ti-Beta-OH crystals are prolate spheres agglomerated together into large clusters (Figure S.4). Characteristic lengths were determined in both the *r* and *z* directions from over 25 individual crystals and averaged to quantify the average surface area and volume per particle.

For materials of consistent zeolite topology, the surface-area-to-volume ratio is an adequate proxy for external surface areas. Surface-area-to-volume ratios per particle were normalized to Ti-Beta-F-155, a representative primary Ti-Beta-F sample studied in this work, assuming a consistent particle density between samples. Table S.3 lists normalized surface-area-to-volume ratios along with normalized silanol densities quantified using IR spectra from CD_3CN titration experiments. A direct correlation between silanol density and external crystal surface area would be expected if all silanols are located only on external crystal surface areas. Silanol densities do not directly scale with surface-area-to-volume ratios, suggesting increased silanol densities present within the microporous environments of Ti-Beta-OH samples.

Table S.3. Surface-area-to-volume (SA/V) ratios and silanol defect densities for selected Ti-Beta-F and Ti-Beta-OH samples normalized to Ti-Beta-F-155.

Sample	Normalized SA/V	Normalized Silanol Density
Ti-Beta-F-135	0.5	0.45
Ti-Beta-F-155	1.0	1.0
Ti-Beta-F-180	0.5	0.86
Ti-Beta-OH-46	18	3.6
Ti-Beta-OH-34	10	3.5
Ti-Beta-OH-71	10	4.1

S.2. Characterization of the hydrophobic properties of Ti-Beta zeolites

S.2.1. Vapor-phase adsorption isotherms on titanosilicate samples

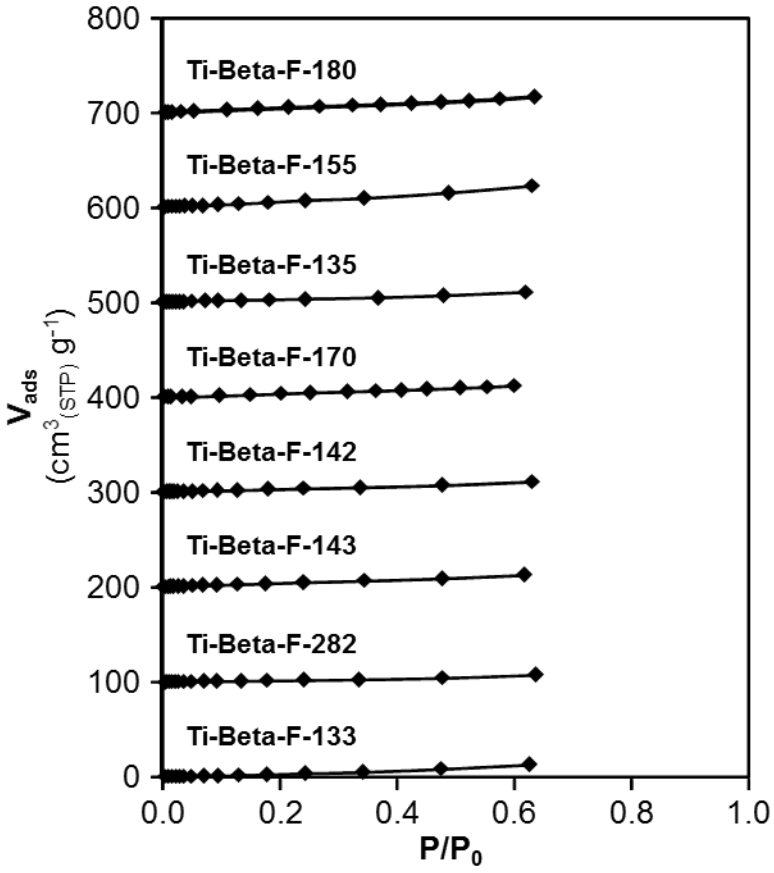

Figure S.16. Vapor-phase water adsorption isotherms at 293 K on Ti-Beta-F samples studied in this work. Isotherms are offset by 100 cm^3 g^{-1} for clarity.

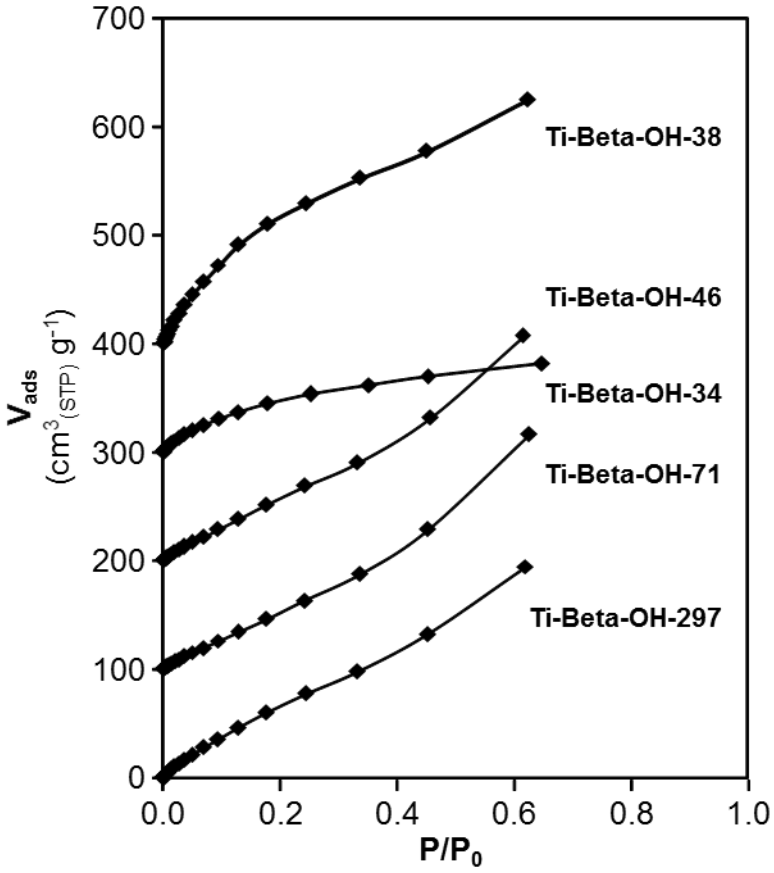

Figure S.17. Vapor-phase water adsorption isotherms at 293 K on Ti-Beta-OH samples studied in this work. Isotherms are offset by 100 cm^3 g^{-1} for clarity.

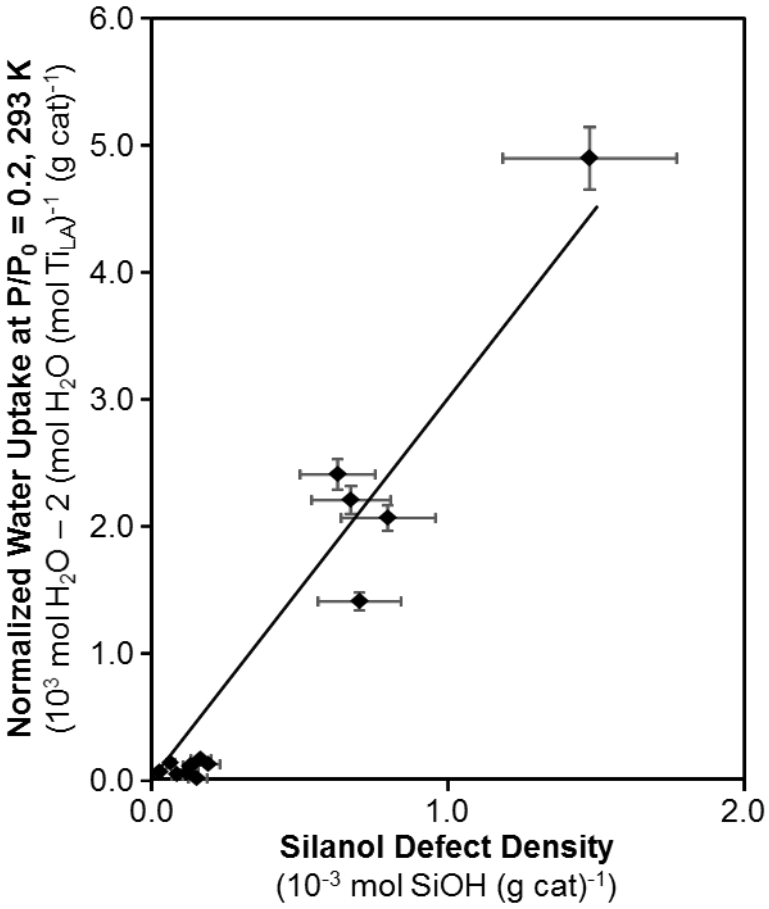

Figure S.18. Water uptakes at $P/P_0 = 0.2$ (373 K) after subtracting two moles of water molecules per mol Ti Lewis acid site (quantified by CD_3CN IR) as a function of the bulk silanol defect density (quantified by CD_3CN IR). The solid line is a best fit line drawn through the origin to guide the eye.

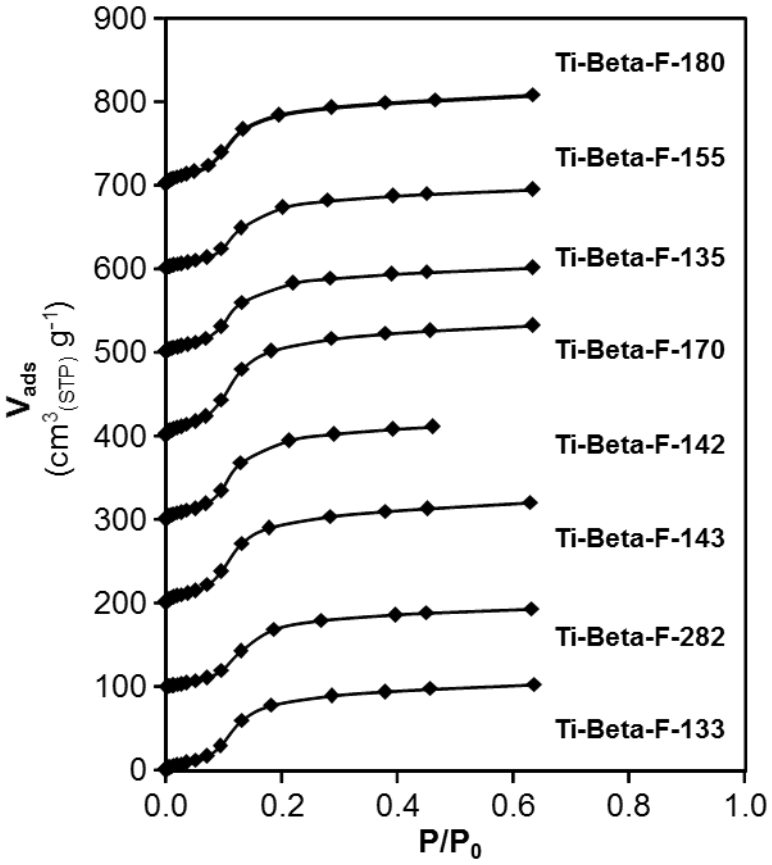

Figure S.19. Vapor-phase methanol adsorption isotherms at 293 K on Ti-Beta-F samples studied in this work. Isotherms are offset by 100 cm^3 g^{-1} for clarity.

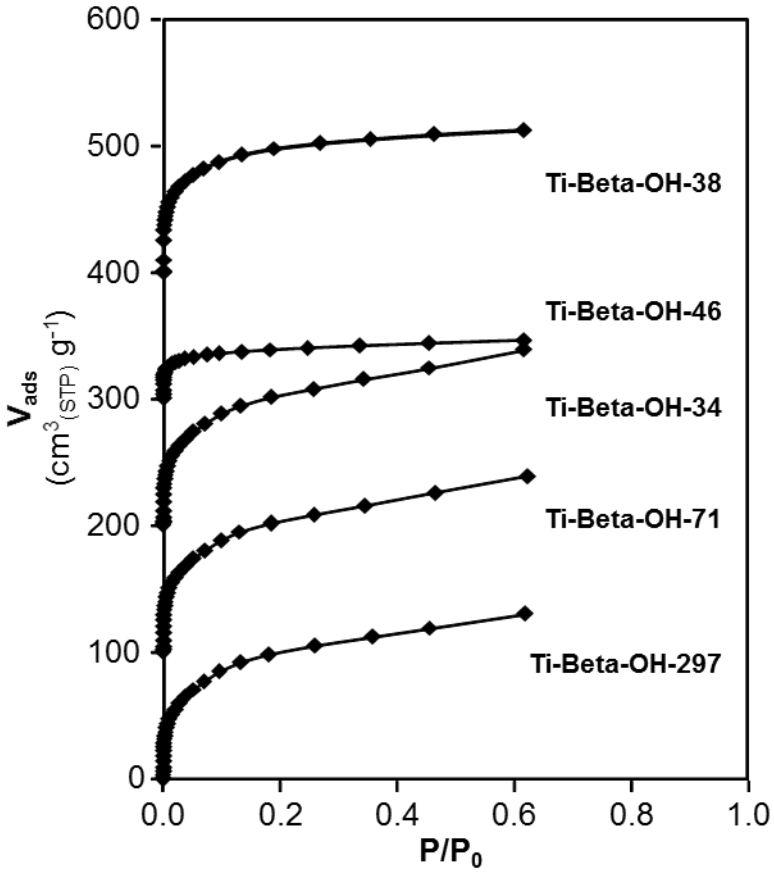

Figure S.20. Vapor-phase methanol adsorption isotherms at 293 K on Ti-Beta-OH samples studied in this work. Isotherms are offset by 100 cm^3 g^{-1} for clarity.

S.2.2. Spectroscopic characterization of intraporous water structures using transmission IR

IR spectra of Ti-Beta-F-155 and Ti-Beta-OH-46 with increasing amounts of gas-phase water exposure are shown in Figures S.21 and S.23 that correspond to Figures 2A and 2B in the main text. Peaks centered between 2700-3800 cm^{-1} and 1550-1750 cm^{-1} increase systematically with increasing water partial pressure which can be equated to an adsorbed water density using the adsorption isotherms given in Figure S.22.

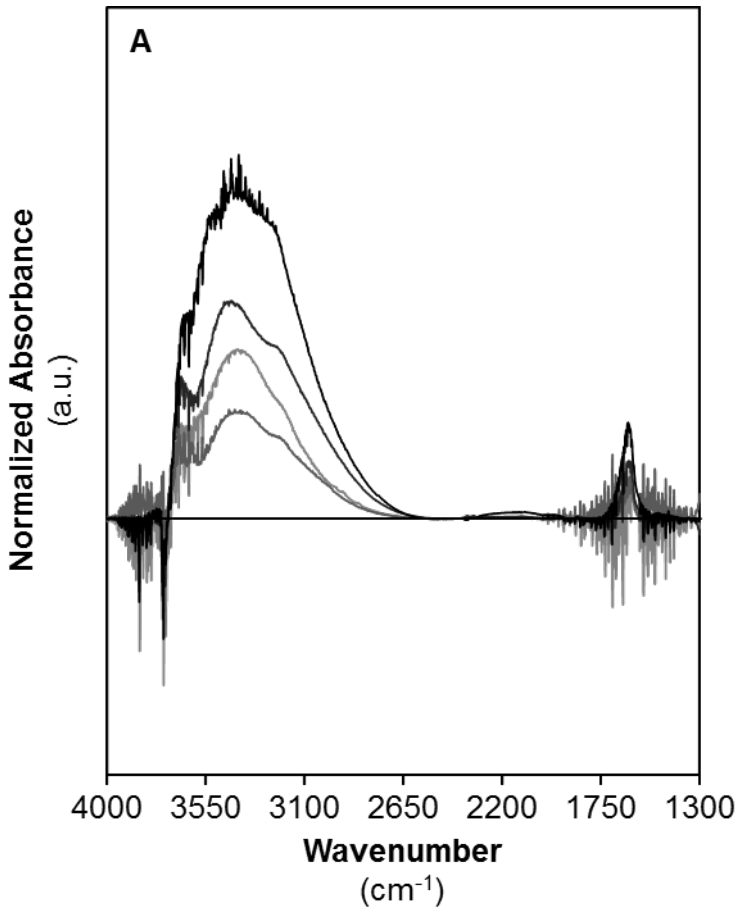

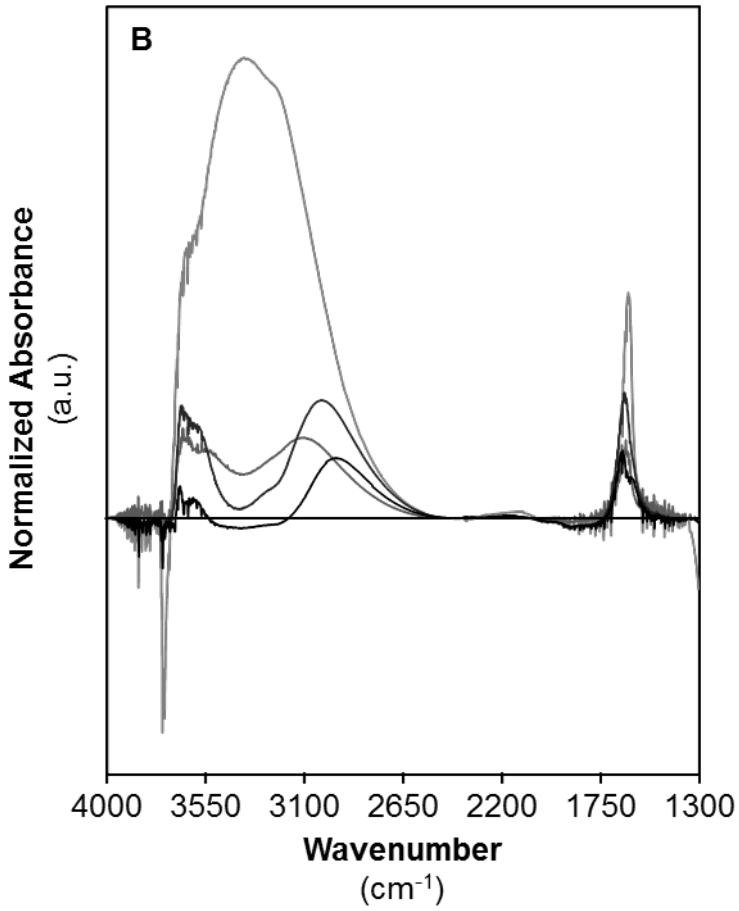

Figure S.21. Differential, subtracted, normalized, cell-corrected IR spectra of adsorbed H_2O at P/P_0=0.1, 0.2, 0.5, and 0.75 (lightest to darkest, 298 K) on (A) Ti-Beta-F-155 and (B) Ti-Beta-OH-46. Differential spectra are spectral changes between a given P/P_0 value and the previous relative pressure spectra, isolating changes in spectral features due only to increasing water partial pressure.

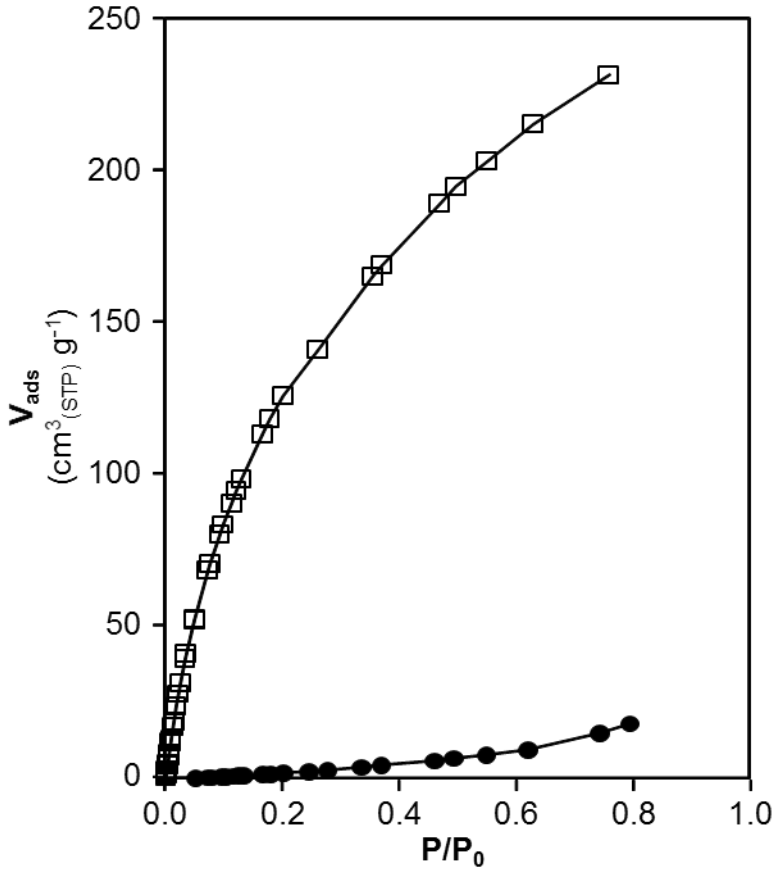

Figure S.22. Vapor-phase water adsorption isotherms at 298 K on Ti-Beta-F-155 (●) and Ti-Beta-OH-46 (□).

Figure S.23 show IR subtraction spectra focusing on the OH stretching region where peaks corresponding to perturbed silanols are observed at 3735 and 3745 cm^{-1}. Spectra collected on Ti-Beta-F-155 observes a continuous increase in perturbed silanol peak area while perturbed silanol peaks observed on Ti-Beta-OH-46 are saturated at lower water partial pressures.

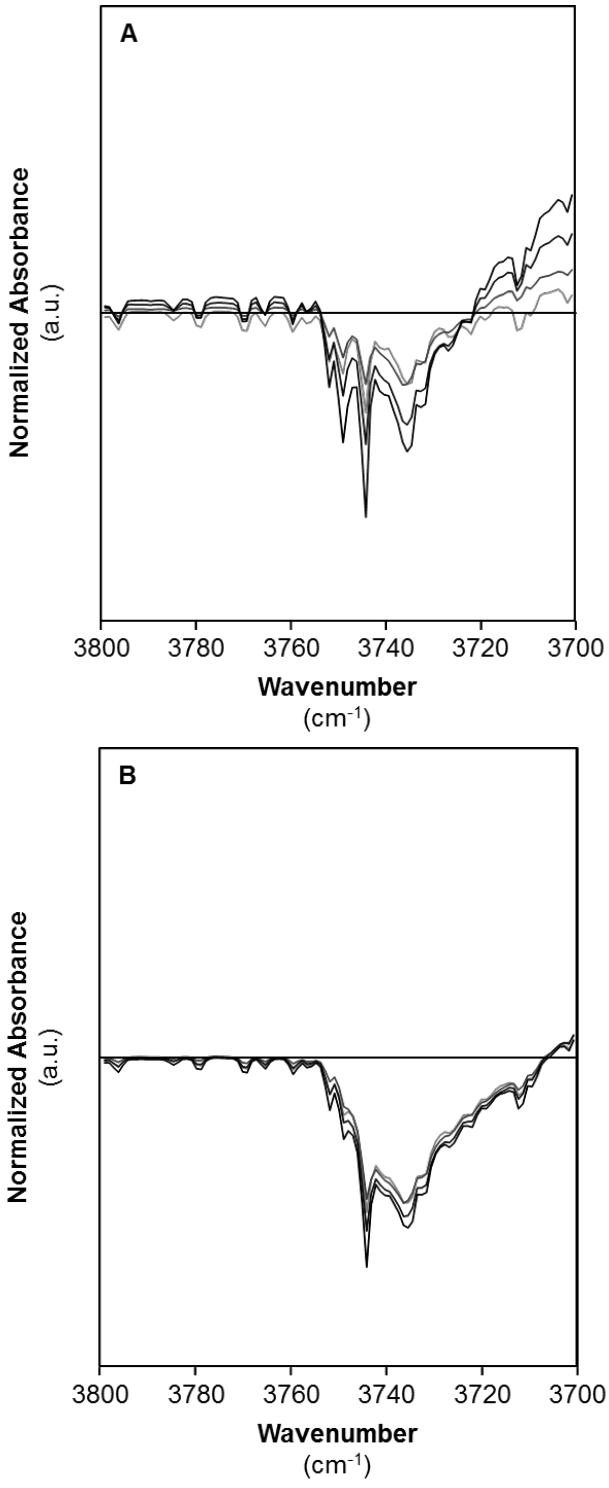

Figure S.23. Subtracted IR spectra of the OH stretching region as a function of increased relative pressure of water on (A) Ti-Beta-F-155 and (B) Ti-Beta-OH-46.

S.3. Glucose isomerization mechanisms and kinetic measurements

S.3.1. Identification of fructose and sorbose formed via glucose isomerization on Ti-Beta zeolites

Isomerization product identification was performed using solution phase ^{13}C NMR as seen in Figure S.22 on representative Ti-Beta-F and Ti-Beta-OH samples. Glucose, fructose, and sorbose standards are shown for comparison. The resonances at $\delta = 61.6$ and 67.3 ppm are peaks indicative of sorbose and fructose respectively and used to confirm isomerization products formed on all samples.

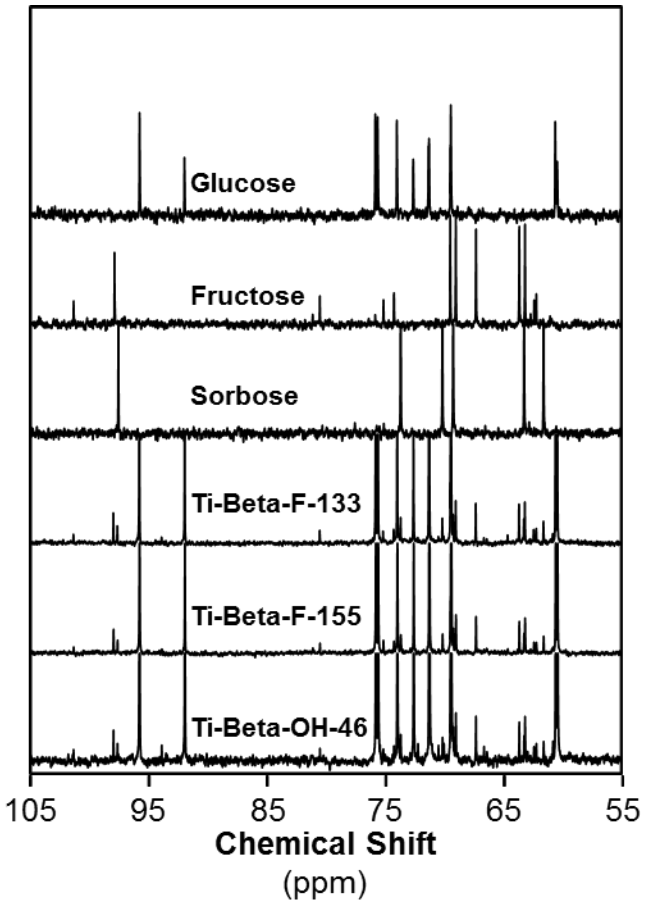

Figure S.24. Solution phase ^{13}C NMR of monosaccharide solutions after contacting 5 wt% glucose solutions with Ti-Beta-F-133, Ti-Beta-F-155, and Ti-Beta-OH-46. Glucose, fructose and sorbose standards are given for direct comparison.

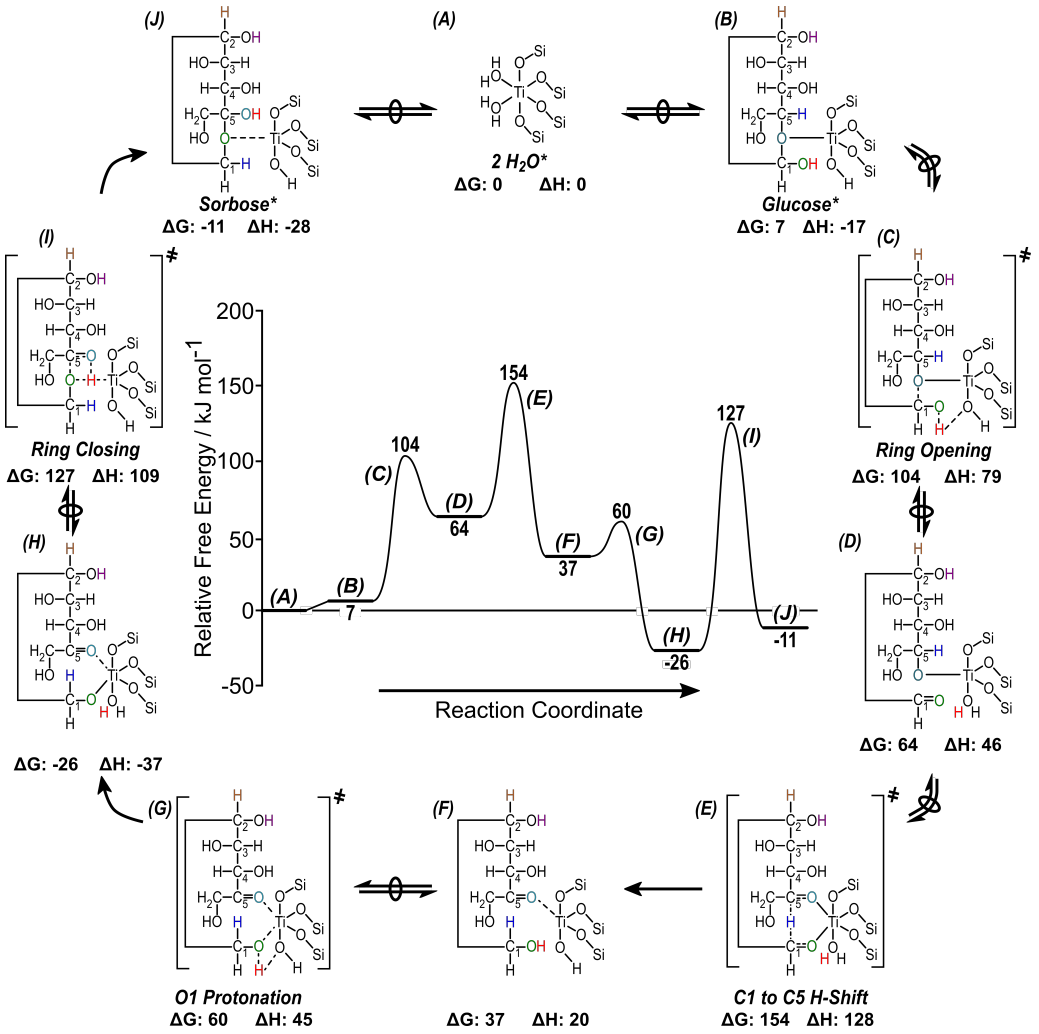

Figure S.25. Free energy (373 K, 1 bar) reaction coordinate diagram for the formation of sorbose from glucose on closed-form Ti Lewis acid sites. Reaction arrows with overlaid circles indicate quasi-equilibrated events or the formation of transition states from relevant precursors. Relative enthalpies are given near inset images.

S.3.2. H/D KIE derivation as a function of temperature for a general vibrational frequency using zero point energies

The H/D KIE measures the apparent rate constant ratio resulting from isotopically labeling an atom located in a kinetically relevant bond which is the alpha C-H bond in the case of Lewis acid mediated glucose-to-fructose isomerization. The apparent isomerization rate constant in the first-order regime can be written as a series of coupled rate constants which reflects free energy differences between the hydride shift transition state with two free water molecules and the water dimer surface intermediate with a single free glucose molecule in solution as follows:

$$k_{first,i} = \frac{K_1 k_2}{K_4 K_5} = \frac{k_B T}{h} e^{(-((\Delta G^o_{\ddagger} + 2\Delta G^o_W) - (\Delta G^o_{G,i} + \Delta G^o_{2W*}))/RT)} \quad \text{(S.1)}$$

Taking the ratio of rate constants, defined as the KIE, for glucose-H2 and glucose-D2 and canceling constants yields the following equation, which relates free energy differences between reaction rates with and without isotopic labeling:

$$KIE = \frac{k_{first,H2}}{k_{first,D2}} = \frac{e^{(-((\Delta G^o_{\ddagger} + 2\Delta G^o_W) - (\Delta G^o_{G,H2} + \Delta G^o_{2W*}))/RT)}}{e^{(-((\Delta G^o_{\ddagger} + 2\Delta G^o_W) - (\Delta G^o_{G,D2} + \Delta G^o_{2W*}))/RT)}} \quad \text{(S.2)}$$

Relevant free energy terms can then be separated between water-dependent and water-independent terms, where water-dependent terms are not affected by isotopically labeling the glucose reactant molecule and thus are irrelevant for observed KIEs:

$$KIE = \frac{e^{(-(2\Delta G^o_W + \Delta G^o_{2W*})/RT)} e^{(-(\Delta G^o_{\ddagger,H2} - \Delta G^o_{G,H2})/RT)}}{e^{(-(2\Delta G^o_W + \Delta G^o_{2W*})/RT)} e^{(-(\Delta G^o_{\ddagger,D2} - \Delta G^o_{G,D2})/RT)}} = \frac{e^{(-(\Delta G^o_{\ddagger,H2} - \Delta G^o_{G,H2})/RT)}}{e^{(-(\Delta G^o_{\ddagger,D2} - \Delta G^o_{G,D2})/RT)}} \quad \text{(S.3)}$$

Similarly, the transition state free energy is not affected by the isotopic label and the associated shift in reduced mass. Therefore, the KIE reflects the free energy difference between the two ground state energies of glucose-D2 and glucose-H2, respectively, which result from differences in zero point energies between C-H and C-D bonds:

$$KIE = e^{(\Delta G^o_{G,H2} - \Delta G^o_{G,D2})/RT} = e^{(ZPE_{H2} - ZPE_{D2})/k_B T} \quad \text{(S.4)}$$

Here, ZPE_i is the zero point energy for C-H and C-D bonds and k_B is the Boltzmann constant ($1.3806*10^{-23}$ m^2 kg s^{-2} K^{-1}). Substituting in the definition of the ZPE and accounting for the vibrational frequency shift upon isotopic labeling ($\nu_D=0.74\nu_H$), the following is derived to define the following generalized KIE equation:

$$\frac{k_{first,H2}}{k_{first,D2}} = e^{(\frac{1}{2}ch\nu_H - \frac{1}{2}ch\nu_D)/k_BT} = e^{(0.13ch\nu_H)/k_BT} \quad \text{(S.5)}$$

where c is the speed of light in a vacuum ($2.998*10^8$ m s^{-1}) and h is the Planck constant ($6.626*10^{-34}$ m^2 kg s^{-1}). This equation yields a KIE value of 2.1 at 373 K for a C-H bond scissoring vibration (ν_H=1500 cm^{-1}) and 4.5 at 373 K for a C-H stretching vibration (~3000 cm^{-1}) corresponding to the kinetically relevant vibrational mode for the Lewis acid and Lewis base catalyzed transition state, respectively. In the case of severe internal mass transfer limitations, the apparent rate constant ratio is equal to the square root of the intrinsic ratio, yielding lower observed KIE values. In this case, the apparent KIE value for a C-H bond scissoring vibration (intrinsic KIE of 2.1) at 373 K would equal a value of 1.4.

$$\left(\frac{k_{first,H2}}{k_{first,D2}}\right)_{app} = \sqrt{\frac{k_{first,H2}}{k_{first,D2}}} \quad \text{(S.6)}$$

The effect of severe internal mass transfer limitations on observed KIEs is independent of the kinetic regime and holds with measured KIE values (2.1-2.3) in both first-order and zero-order regimes.

The apparent lack of mass transfer reflected by experimentally measured KIE values of 2.1 is supported by consistent glucose isomerization rates for fructose and sorbose formation normalized per total Ti content (Figure 4, main text) and as a function of Lewis acidic Ti content (Figure S.26).

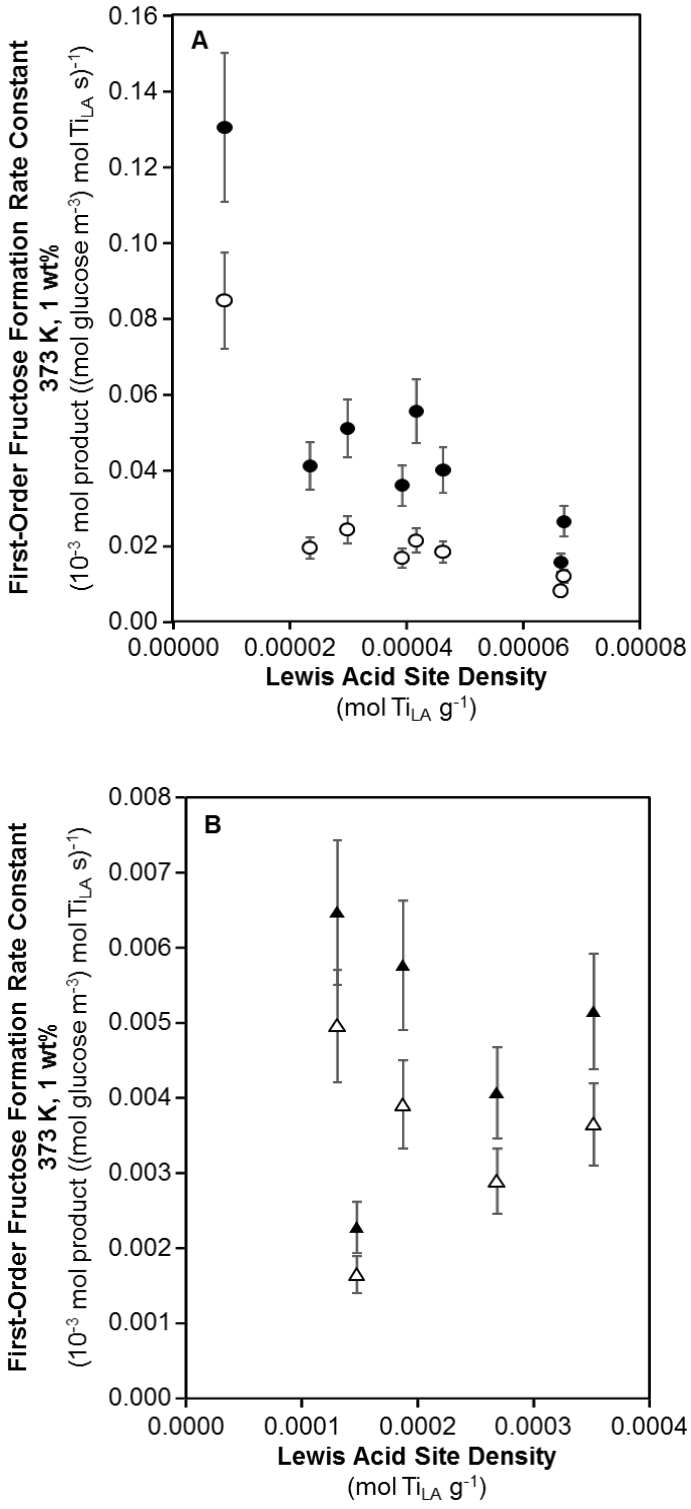

Figure S.26. First-order fructose (●, ▲) and sorbose (○,△) formation rate constants (373 K, pH 4) normalized per total Lewis acidic Ti content (measured from CD_3CN IR) as a function of Lewis acidic Ti density for (A) Ti-Beta-F and (B) Ti-Beta-OH samples.

S.3.3. Bulk solution glucose and osmotic activity coefficient quantification

Standard state glucose activity coefficients (298 K), osmotic coefficients, and excess partial molar enthalpies were linearly interpolated from literature values as a function of glucose mole fraction where activity coefficients vary from unity to 1.329 (298 K) at high glucose concentrations approaching the aqueous room temperature solubility of glucose [1]. Interpolated activity coefficients were then adjusted to reaction temperature using the following thermodynamic relationship [2]:

$$\frac{-\bar{H}_i^E}{RT^2} = \frac{\partial}{\partial T} \ln(\gamma_i) \tag{S.7}$$

Here, $\bar{H}_i^E$ is the excess partial molar enthalpy of species *i* in solution, R is the universal gas constant, T is absolute temperature in K, and γ_i is the activity coefficient of species *i* in solution which is a function of temperature and the concentration of species *i*. Excess partial molar enthalpies are assumed to be independent of temperature across the studied temperature range. Eq. (S.7) can be integrated into:

$$\gamma_i = \gamma_i^0 e^{\frac{\bar{H}_i^E}{R}\left(\frac{1}{T} - \frac{1}{T^0}\right)} \tag{S.8}$$

Here, γ_i and γ_i^0 are the activity coefficients of species i at the reaction temperature and standard temperature (298 K) respectively, and T and T^0 are the reaction and standard state absolute temperatures respectively. Glucose and osmotic activities at reaction conditions were then calculated from the initial concentrations of glucose and water multiplied by the temperature-adjusted osmotic or activity coefficient as appropriate. We note that all kinetic trends hold constant independent of whether concentrations or thermodynamic activities (using activity coefficients quantified at either 298 K or reaction temperatures, see Figure S.27 and Section S.5.2 below) are used for glucose and water species. In the main text, temperature-adjusted activities are used as an accurate descriptor in the rate equation models.

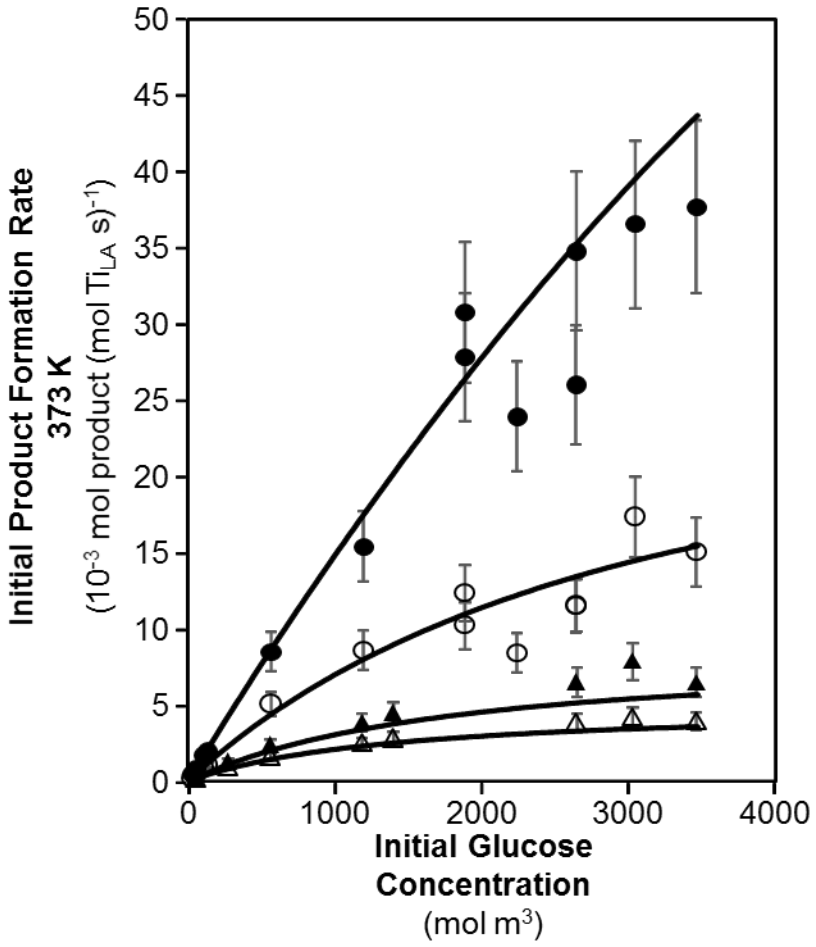

Figure S.27. Dependence of initial glucose isomerization rates (373 K, pH 4) for fructose (filled) and sorbose (open) formation on Ti-Beta-F-155 (●, ○) and Ti-Beta-OH-46 (▲, △) as a function of initial glucose concentration (1-50 wt%). Solid lines represent fits of the experimental data to the rate equation (Eq. (9) of the main text) using activation enthalpies and entropies given in Table 4.

S.4. Characterization and kinetic effects of bound surface species in first-order and zero-order regimes

S.4.1. ATR-IR and modulation excitation spectroscopy quantification for the identification of bound reactive intermediates using MCR-ALS data analysis techniques

The time-resolved FTIR spectra for each Beta material were collected and processed mathematically prior to analyzing spectral features of individual species. The time-domain raw spectra were first averaged into a single period using:

$$A_{average}(t) = \frac{T}{T_{total}} \sum_{i=0}^{\frac{T_{total}}{T}} A(t + iT) \tag{S.9}$$

Here $A(t + iT)$ is the absorbance at each time point, $A_{average}(t)$ is the absorbance after averaging into a single period, T is the time period of stimulation, and T_{total} is the total time for which the experiment was run; therefore, $\frac{T_{total}}{T}$ represents the total number of periods measured during a MES experiment. The averaged spectra were then subjected to phase sensitive detection (PSD) using:

$$A_k\left(\varphi_k^{PSD}\right) = \frac{2}{T}\int_0^T A_{average}(\vartheta, t)\sin\left(k\omega t + \varphi_k^{PSD}\right)dt \tag{S.10}$$

Eq. (S.10) was transformed into a Fourier series by Fourier's theorem for a periodic function gives:

$$A(\vartheta, t) = \sum_{i=1}^{N} A_{i,0}(\vartheta) + \sum_{i=1}^{N}\sum_{k=1}^{\infty}\left(A_{i,k}^{0^\circ}(\vartheta)\cos k\omega t + A_{i,k}^{90^\circ}(\vartheta)\sin k\omega t\right) \tag{S.11}$$

where $A_{i,0}$ is the dc component, and $A_{i,k}^{0^\circ}$ and $A_{i,k}^{90^\circ}$ are the orthogonal components of the vector. Each of the above terms in the integral was converted into a single equation using Simpson's Rule:

$$\int_0^T y(t)dt = \frac{\Delta t}{3}(y_0 + 4y_1 + 2y_2 + 4y_3 + \cdots + 2y_{n-2} + 4y_{n-1} + y_n) = \frac{\Delta t}{3}\sum_{i=0}^{n} s_i y_i \quad \text{(S.12)}$$

where s_i, is Simpson's coefficient (where n must be an even number). A detailed mathematical derivation and implications are discussed in detail elsewhere [3]. A self-developed MATLAB code reported previously [4] was used to resample and average the time resolved spectra and then perform the PSD calculations described in Eqs. (S.11) and (S.12) to yield the phase domain spectra. Figures S.28 show an example of the time resolved and phase resolved spectra for Ti-Beta-F-155.

Phase resolved spectra were then subjected to MCR-ALS to extract independent species, including the surface coverages and spectra. Spectra were truncated to contain wavenumbers 3800-2600 and 1800-700 cm^{-1} and phase angles 1-181^o to reduce data set size into MATLAB. Singlular value decomposition suggests only two independent species to fully describe the phase resolved spectra. Two sine wave functions were input for the initial guess of the surface coverages and the spectra were constrained to solve for positive features. The MATLAB program iteratively solved for spectra and surface coverages until the convergence criteria were met and the sum of residuals was less than 10^{-16}. The resulting spectra were smoothed with a Fourier Transform filter, baseline corrected, and normalized to the most intense feature between 1000 and 1150 cm^{-1} using OriginLab's OriginPro 9 software. Initial guesses of three or more species yielded solutions of zero for spectra and surface coverages of all species after two, further indicating that the phase resolved spectra can be completely described by just two independent species.

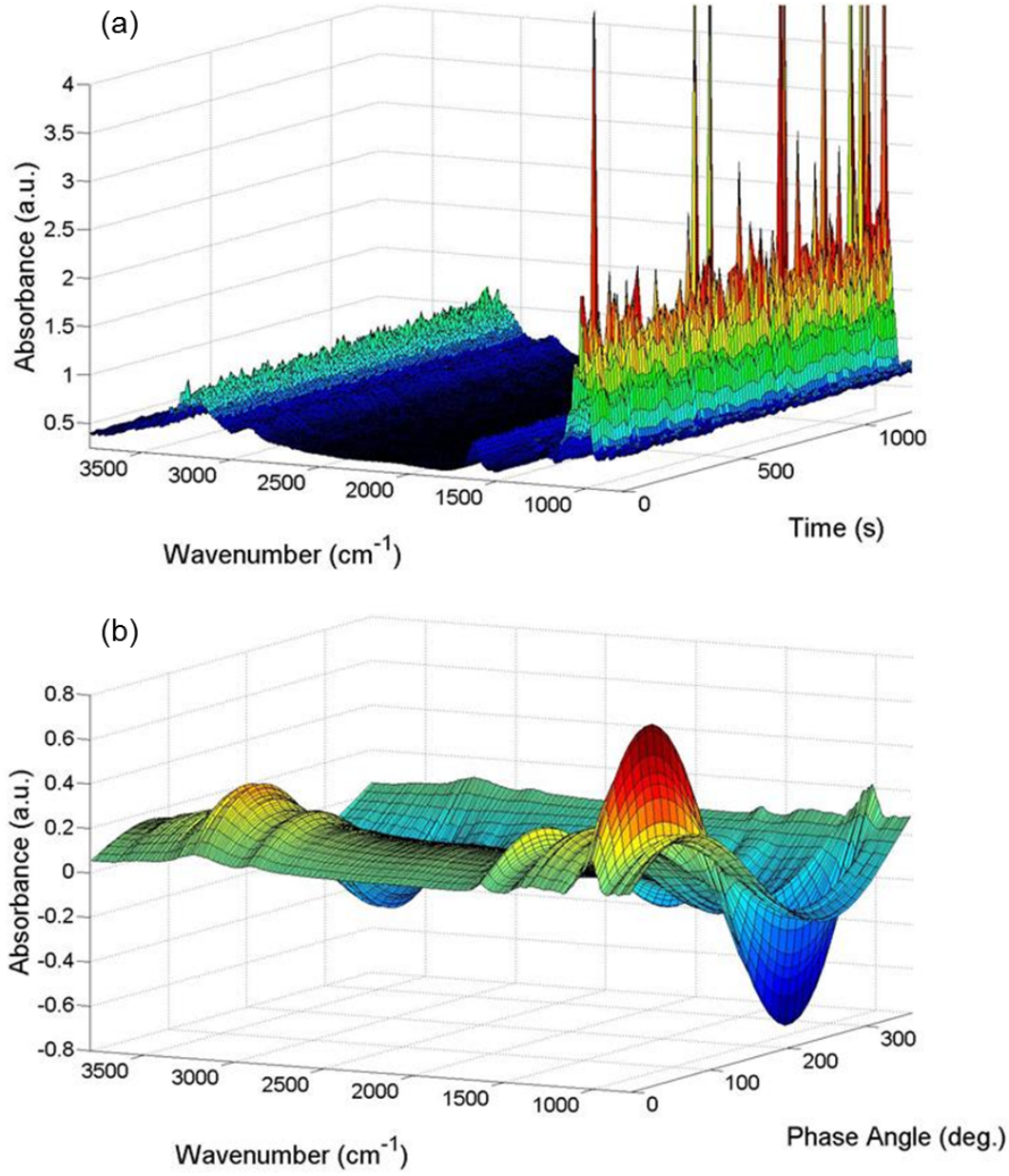

Figure S.28. a) Time-resolved infrared spectra obtained *in situ* during reactions of glucose and water over Ti-Beta-F-155 while modulating glucose concentrations (42-50 wt%) with a period length of 250 s at 373 K. b) Phase resolved spectra that result from phase sensitive detection of the time resolved spectra in (a). Coloring indicates absorbance intensity.

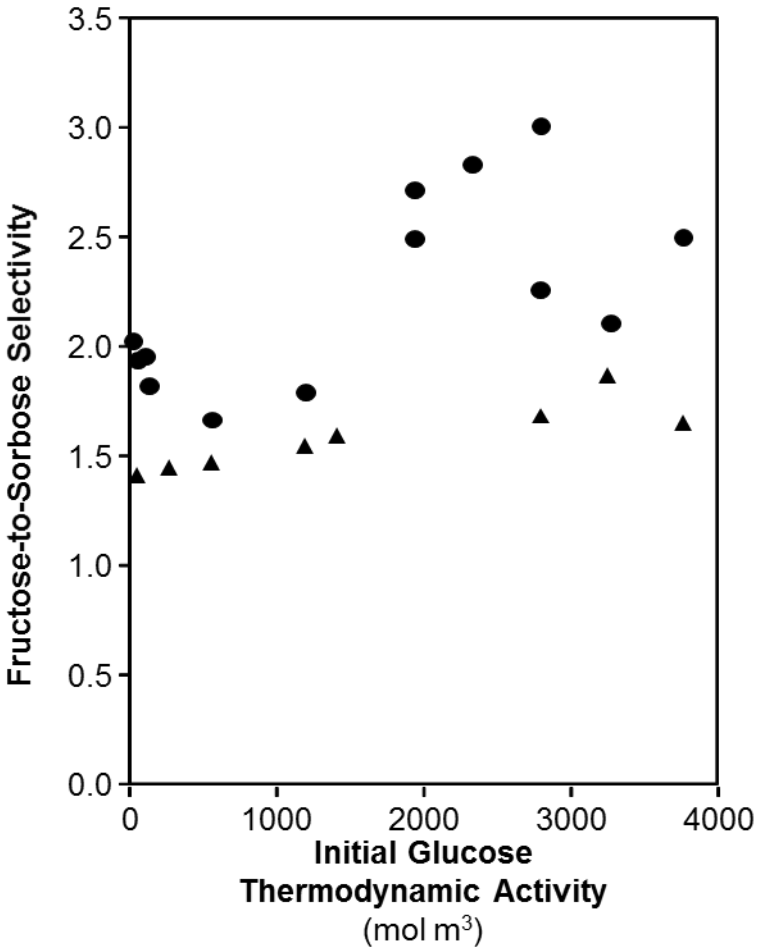

Figure S.29. Dependence of fructose-to-sorbose selectivity (373 K, pH 4) on Ti-Beta-F-155 (●) and Ti-Beta-OH-46 (▲) as a function of initial glucose thermodynamic activity. Relatively constant product selectivities support the identification of the secondary bound glucose species being a bound intermediate which is not directly responsible for sorbose formation as relative coverages of MARI and secondary bound species observed from ATR-IR are affected by changes in initial glucose activity.

S.4.2. Comparison of bound glucose intermediates from ATR-IR spectra and DFT calculations

Spectra of glucose derived intermediates shown in Figure 6B (main text) differ from previous reports of glucose-derived bound to framework Sn atoms in Sn-Beta zeolites from IR spectra; however, the differences are unsurprising given the methods of acquiring each spectra. Previous work characterized glucose derived intermediates measured ex situ within dried zeolites. Such experiments revealed a carbonyl feature at 1728 cm^{-1}, a lack of δ(O-H) at 1630 cm^{-1} due to the absence of the solvent, and a different series of features between 1200-1500 cm^{-1}.[5] Intuition and comparisons of the previous results to those in Figure 6 show that samples studied ex situ (and following dehydrations) do not result in similar charge transfer between intermediates and the Lewis acidic active site and do not reflect hydrogen bonding interactions associated with aqueous solvent. Spectra obtained in situ using ATR-IR shown in Figure 6B (main text) accurately reflect these consequential interactions and correspond to reactive intermediates that may be catalytically relevant instead of fluid phase reactants or inactive, persistent residues.

The structure of glucose-derived MARI species is characterized by complex vibrational modes particularly between 900 and 1200 cm^{-1}, which previous studies have partially deciphered.[6-8] Measured spectra of aqueous-phase glucose over the ZnSe crystal also contains a feature at 1024 cm^{-1} that is attributed to the same C_1-O_5-C_5 ring breathing mode and is absent in all of the spectra of glucose-derived intermediates over Ti-Beta catalysts (Figure 6B, main text). DFT-calculated ring-closed glucose structures bound to Ti sites show a vibrational frequency at 1033 cm^{-1} (Movie S.1, Supp. Info.) that includes C_1-O_5-C_5 ring breathing modes, which are absent in DFT-calculated ring-opened structures in the gas-phase and within zeolite pores. Thus, glucose observed over the ZnSe crystal exists predominantly in a ring-closed conformation yet

the absence of these resonances upon adsorption onto Lewis acidic Ti sites may reflect the presence of ring-opened intermediates.

Further analysis of the bound glucose species can be performed by examining the feature at 1005 cm^{-1} which is present in the spectra reflecting both the MARI and the minor species on Ti-Beta-OH-46, but absent in spectra reflecting the MARI and minor species on Ti-Beta-F-155. DFT-calculated vibrations of reactive intermediates that form fructose show vibrations at 1002 or 1004 cm^{-1} (Movies S.3 and S.4, respectively, Supp. Info.) when silanol groups are located near the Ti active site; however, reactive intermediates that lead to fructose in a defect-free Ti-Beta pore do not show vibrational modes near 1004 cm^{-1}. The correlation between the vibrations near 1004 cm^{-1} in intermediates that lead to fructose and the existence of defect sites (or silanol groups) near the Ti active site suggest the vibrations observed at 1004 cm^{-1}, which result from coordinated ν(C-C) and δ(C-H) modes, must result from interactions with the silanol groups within Beta pores. Differences in these interactions with proximal silanol groups are consistent with the different silanol densities present between the hydrophilic Ti-Beta-OH-46 and hydrophobic Ti-Beta-F-155 samples (Table 2, main text). Alternatively, these spectral differences may also reflect interactions with nearby hydroxyl groups formed by in situ interconversion of closed (four framework bonds) to open (three framework bonds and one hydroxyl ligand) Ti sites. These hydroxyl groups may hydrogen bond with adsorbed species and cause vibrational modes to appear at 1004 cm^{-1}. These differences between the observed reactive intermediates over Ti-Beta-OH-46 and Ti-Beta-F-155 indicate that hydrophilic and hydrophobic pore environments may stabilize different reactive intermediates that both form fructose, as spectra reflecting both MARI and minor intermediates lack the carbonyl expected in sorbose precursors and may further lead to the measured differences in rates (Figure 5, main text).

S.4.3. Ti structural characterization using XAS and DFT

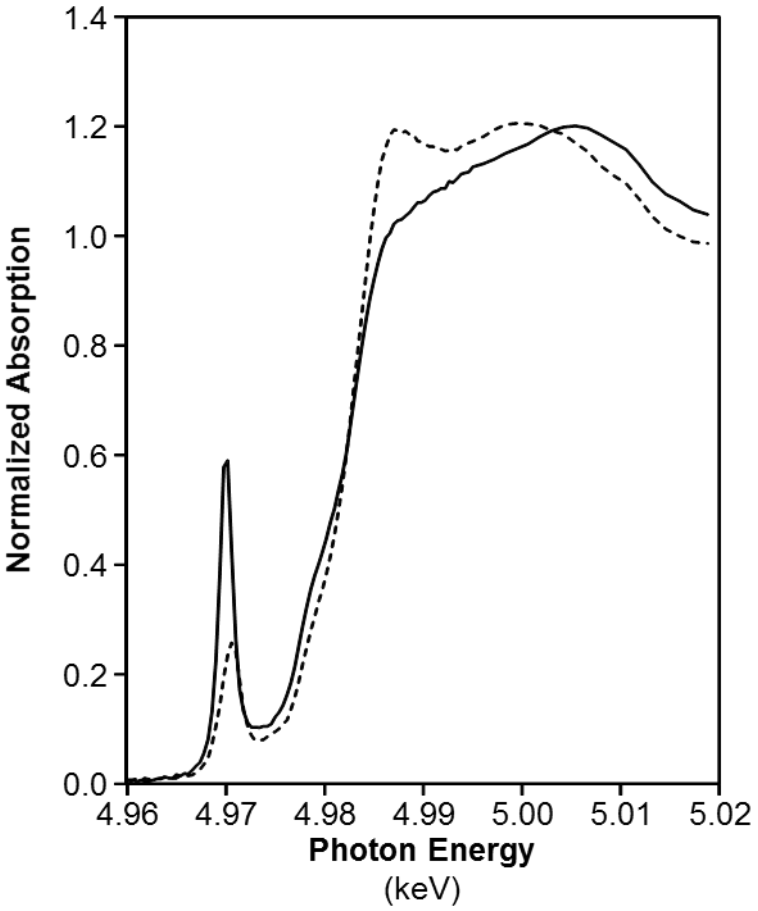

Figure S.30. Ti K edge XANES of water exchanged Ti-Beta-OH-46 zeolite after dehydration at 523 K in He (solid) and under ambient conditions (dashed). The increase in intensity of the pre-edge peak is consistent with a decrease in coordination number from 6 to 4 upon dehydration.

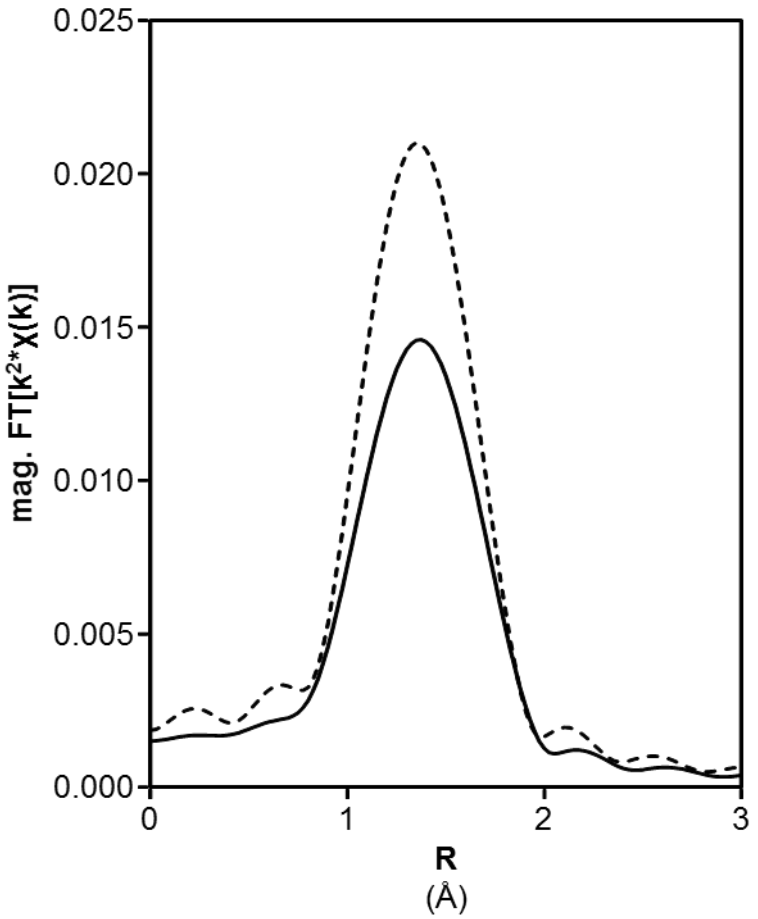

Figure S.31. Magnitude of the Fourier transform of the k^2-weighted Ti K edge EXAFS of water exchanged Ti-Beta-OH-46 zeolite under ambient conditions (solid) and after dehydration at 523 K in He (dashed).

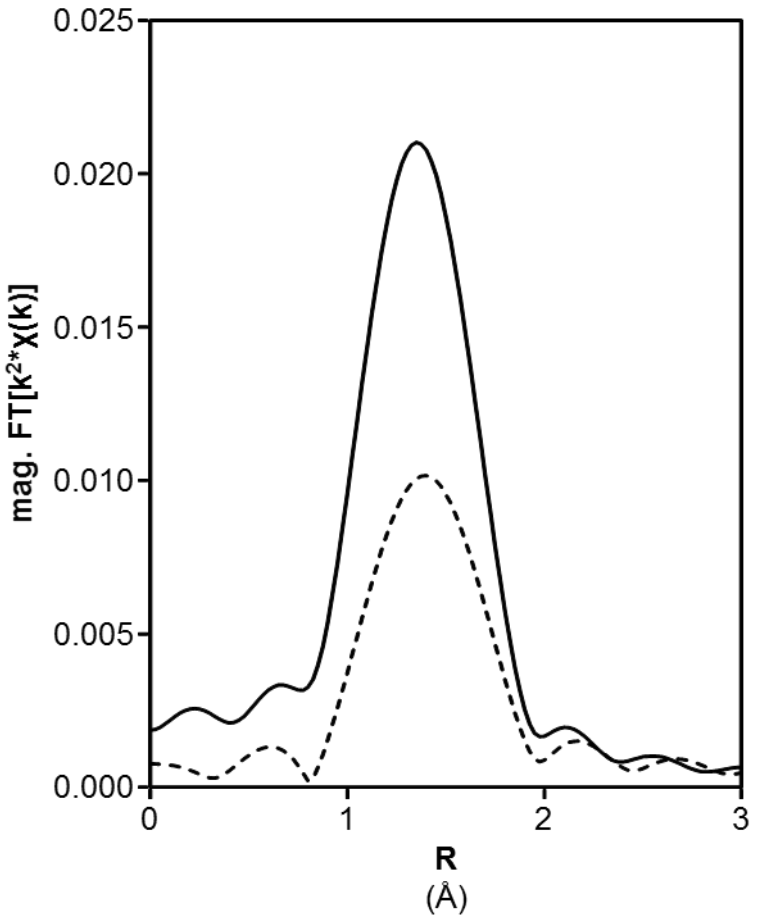

Figure S.32. Magnitude of the Fourier transform of the k^2-weighted Ti K edge EXAFS of water exchanged Ti-Beta-OH-46 zeolite after dehydration at 523 K in He (solid) and ΔEXAFS of the hydrated and dehydrated water exchanged catalyst (dashed). The ΔEXAFS spectrum was obtained by subtracting the k^0-weighted EXAFS of the sample after dehydration from the k^0-weighted EXAFS of the sample under ambient conditions and is representative of the water adsorbed on Ti under ambient conditions.

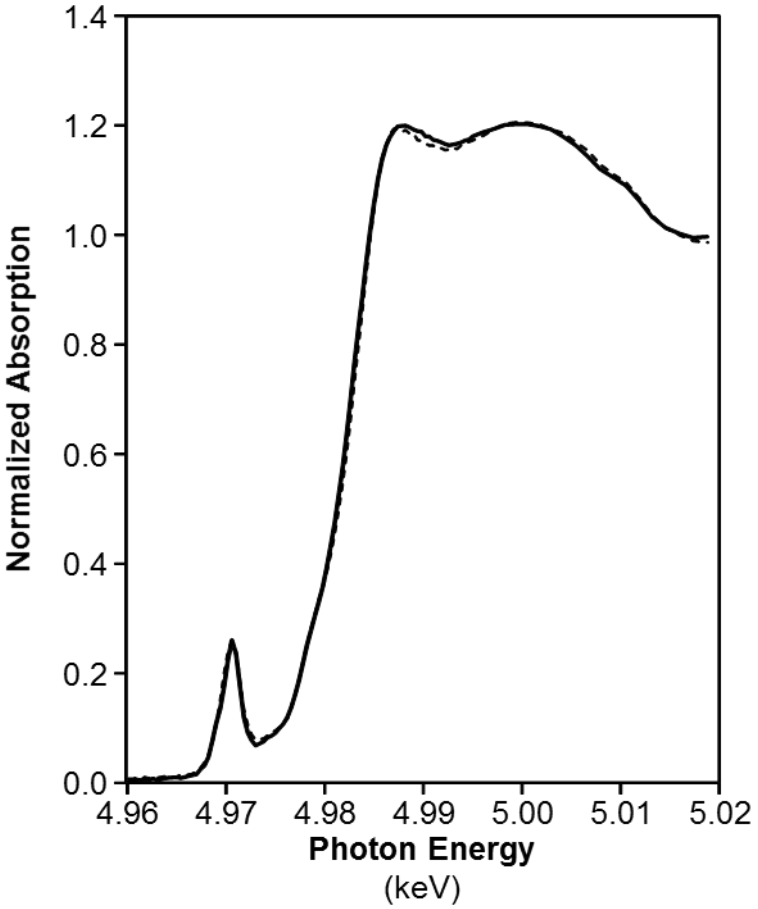

Figure S.33. Ti K edge XANES of water (dashed) and glucose (solid) exchanged Ti-Beta-OH-46 zeolite under ambient conditions. The spectra are identical within experimental error indicating Ti has equivalent coordination environments in the two samples. The intensity of the pre-edge peak is consistent with a coordination number of 6.

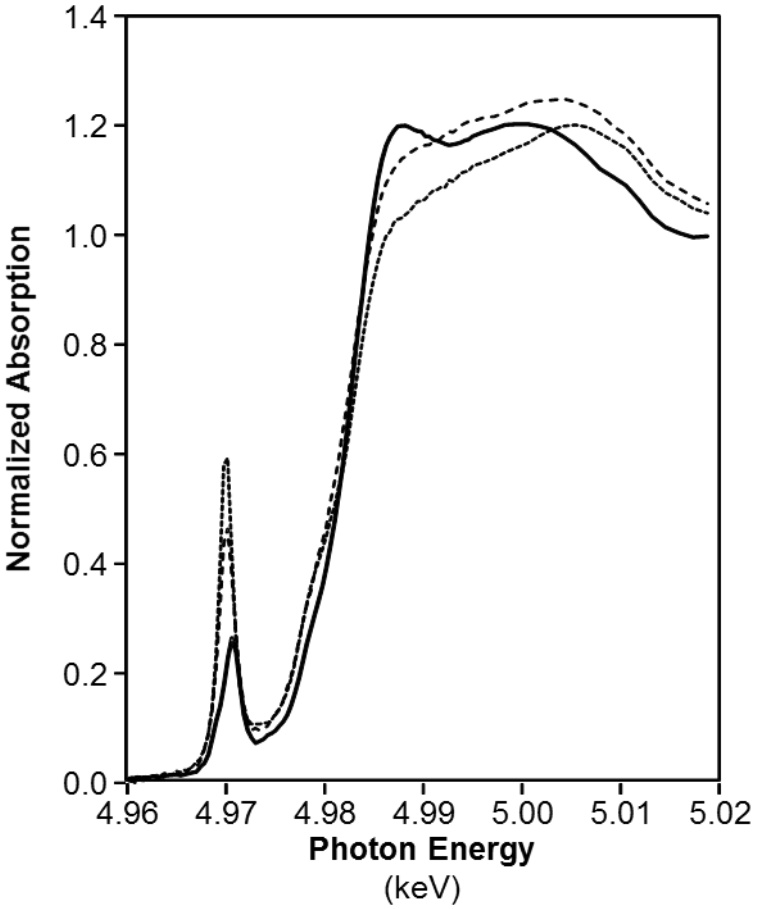

Figure S.34. Ti K edge XANES of Ti-Beta-OH-46 zeolite: solid – glucose exchanged under ambient conditions, long dashes – glucose exchanged after treatment at 523 K in He, and short dashes – water exchanged after treatment at 523 K in He. The intensity of the pre-edge peak in the glucose exchanged sample after treatment in He at 523 K is consistent with a coordination number of 5 and suggests glucose adsorbed through a single oxygen.

The Ti-O coordination number of 4 obtained from fitting the EXAFS of the sample after dehydration is consistent with the intense XANES pre-edge peak at 4.9700 keV and the presence of tetrahedral Ti in the zeolite framework. The pre-edge peak in the hydrated sample is less intense and shifted to higher energy (4.9707 keV) than the hydrated sample and is consistent with a Ti coordination number of 6 [9]. However, the magnitude of the Fourier transform of the k^2-weighted EXAFS of the hydrated sample is lower than the dehydrated catalyst. Fitting the EXAFS of the hydrated sample with a single Ti-O path gives a coordination number of 3.8, lower than the value of 6 expected from the XANES, and a bond distance of 1.85 Å. Satisfactory fits of the hydrated and dehydrated spectra were obtained with Debye-Waller factors ($\Delta\sigma^2$) of $1.0*10^{-3}$ and $-2.0*10^{-3}$ $Å^2$, respectively. The higher $\Delta\sigma^2$ indicates a larger distributions of Ti-O bond distances under ambient conditions than after dehydration. This suggests that the fitted coordination number of 3.8 is a result of destructive interference between Ti-O scattering paths of different distances (i.e. $Ti\text{-}O_{framework}$ and $Ti\text{-}O_{water}$).

To determine the number and bond distance of the adsorbed water, a ΔEXAFS spectrum was obtained by taking the difference of the k^0-weighted EXAFS of the ambient and dehydrated samples. In obtaining the ΔEXAFS spectrum it was assumed that the four Ti-O framework bonds in the dehydrated sample are unaffected by the adsorption of water. A Ti-O coordination number of 2 and bond distance of 1.94 Å were obtained from fitting the difference spectrum. Therefore, the total Ti-O coordination number of the hydrated sample is 6, consistent with XANES, at an average bond distance of 1.87 Å, consistent with the single scatter fit of the ambient spectrum.

Table S.4. Ti energies, coordination numbers, and bond distances determined from Ti XAS.

Sample	Pre-edge Energy (keV)	Edge Energy (keV)	Ti-O Coordination Number	Ti-O Bond Distance (Å)	$\Delta\sigma^2$ (10^3 Å^2)	E0 (eV)
Water Exchanged, Dehydrated	4.9700	4.978	4.2	1.83	-2.0	0.3
Water Exchanged, Hydrated (Single scatter fit)	4.9707	4.978	3.8	1.85	1.0	-0.7
ΔEXAFS (ambient – dehydrated)	---	---	2.1	1.94	-3.0	-12
Water Exchanged, Hydrated (Total, two scatter fit)	---	---	4.2	1.83	-2.0	0.3
	---	---	2.1	1.94	-3.0	-12.
Glucose Exchanged, Hydrated	4.9707	4.978	6[a]	---	---	---
Glucose Exchanged, Dehydrated	4.9702	4.978	5[a]	---	---	---

[a] Coordination numbers were determined from the intensity of the pre-edge peak of the Ti K edge XANES spectra. Due to poor data quality in the EXAFS region of the absorption spectra reliable fits of these samples could not be obtained.

S.5. Enthalpic and entropic contributions of hydrophobic reaction pockets for aqueous-phase glucose isomerization

S.5.1. Derivation of mechanism-based rate expressions for glucose isomerization catalyzed by Lewis acid sites

A reaction pathway for the parallel formation of fructose and sorbose from glucose is given in Scheme S.1, identical to Scheme 1 from the main text. Here, $G_{(l)}$, $F_{(l)}$, and $S_{(l)}$ stand for glucose, fructose, and sorbose respectively in the liquid phase, * represents a bare Lewis acid site, G* represent the adsorbed glucose intermediate, $(R^*)_F$ and $(R^*)_S$ represent the bound glucose precursors leading to fructose and sorbose respectively, F* and S* represent bound fructose and sorbose respectively, and K_i is the equilibrium coefficient for Step *i*. $k_{2,i}$ is the rate constant for product formation from the kinetically relevant hydride shift transition state for each product. Sequential water (W) adsorption onto a Lewis acid site forms one (W*) and two (2W*) bound water intermediates (Scheme S.1). This scheme and the rate equation derived from it are similar to that reported in Ref. [10].

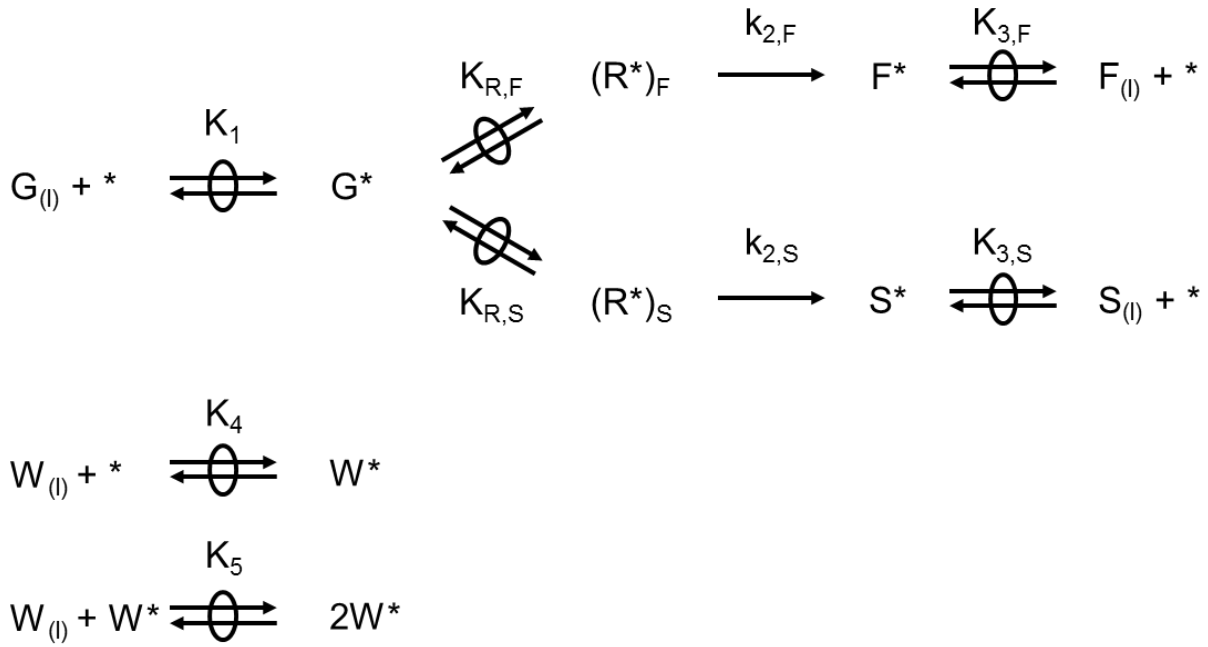

Scheme S.1. Plausible glucose isomerization mechanism for fructose and sorbose formation on Lewis acidic Ti sites, modified from Ref. [10]. Quasi-equilibrated glucose adsorption (Steps 1a, 1b) forms bound glucose intermediates which form bound fructose (Step 2a) or sorbose (Step 2b) isomers through kinetically relevant hydride shifts. Quasi-equilibrated fructose (Step 3a) and sorbose (Step 3b) desorption phenomena release the product into the liquid phase. Quasi-equilibrated water adsorption onto Lewis acidic active sites (Steps 4 and 5) inhibits isomerization rates at low glucose coverages.

In Scheme S.1, sequences F and S reflect glucose isomerization to fructose and to sorbose. Net isomerization rates to fructose ($r_{isom,F}$) and sorbose ($r_{isom,S}$) are given by:

$$r_{isom,F} = r_{2,F} - r_{-2,F} \tag{S.13}$$

$$r_{isom,S} = r_{2,S} - r_{-2,S} \tag{S.14}$$

From the law of mass action, reaction rates of elementary steps are proportional to rate constants (k_i) and concentrations of kinetically relevant transition states ($c_{‡,i}$). Therefore, net reaction rates can be written as:

$$r_{isom,F} = k_{2,F} c_{‡,F} - k_{-2,F} c_{F*} \tag{S.15}$$

$$r_{isom,S} = k_{2,S} c_{‡,S} - k_{-2,S} c_{S*} \tag{S.16}$$

Concentration terms can be related to the thermodynamic activities through the following relationship which references a standard concentration of 1 mol m^{-3}:

$$a_i = \gamma_i \frac{c_i}{c^0} \tag{S.17}$$

Using the definition of activity in Eq. (S.17), Eqs. (S.15) and (S.16) can then be rewritten as:

$$r_{isom,F} = \frac{k_{2,F}}{\gamma_{\ddagger,\mathrm{F}}} a_{\ddagger,F} - \frac{k_{-2,F}}{\gamma_{\mathrm{F}*}} a_{F*} \tag{S.18}$$

$$r_{isom,S} = \frac{k_{2,S}}{\gamma_{\ddagger,\mathrm{S}}} a_{\ddagger,S} - \frac{k_{-2,S}}{\gamma_{\mathrm{S}*}} a_{S*} \tag{S.19}$$

We note that Eqs. (S.18) and (S.19) can rewritten as:

$$r_{isom,F} = \frac{k_{2,F}}{\gamma_{\ddagger,\mathrm{F}}} a_{\ddagger,F}\left(1 - \frac{k_{-2,F} a_{F*} \gamma_{\ddagger,\mathrm{F}}}{k_{2,F} a_{\ddagger,F} \gamma_{\mathrm{F}*}}\right) = \frac{k_{2,F}}{\gamma_{\ddagger,\mathrm{F}}} a_{\ddagger,F}\left(1 - \frac{a_{F*}\gamma_{\ddagger,\mathrm{F}}}{K_{2,F} a_{\ddagger,F} \gamma_{\mathrm{F}*}}\right) \tag{S.20}$$

$$r_{isom,S} = \frac{k_{2,S}}{\gamma_{\ddagger,\mathrm{S}}} a_{\ddagger,S}\left(1 - \frac{k_{-2,S} a_{S*} \gamma_{\ddagger,\mathrm{S}}}{k_{2,S} a_{\ddagger,S} \gamma_{\mathrm{S}*}}\right) = \frac{k_{2,S}}{\gamma_{\ddagger,\mathrm{S}}} a_{\ddagger,S}\left(1 - \frac{a_{S*}\gamma_{\ddagger,\mathrm{S}}}{K_{2,S} a_{\ddagger,S} \gamma_{\mathrm{S}*}}\right) \tag{S.21}$$

or:

$$r_{isom,F} = \frac{k_{2,F}}{\gamma_{\ddagger,\mathrm{F}}} a_{\ddagger,F}(1 - \eta_F) \tag{S.22}$$

$$r_{isom,S} = \frac{k_{2,S}}{\gamma_{\ddagger,\mathrm{S}}} a_{\ddagger,S}(1 - \eta_S) \tag{S.23}$$

Here, η_F and η_S are the approach-to-equilibrium terms for Steps 2F and 2S respectively (Scheme S.1).

The 1,2-hydride shift (or 1,5-hydride shift) step is kinetically relevant for fructose (or sorbose) formation as determined from H/D kinetic isotope effect measurements and isotopic tracer studies [11]. Steps 1F, 1S, 3F, 3S, 4 and 5 are then assumed to be quasi-equilibrated and the following equilibrium expressions are derived to relate thermodynamic activities of reactant and product species:

$$K_1 = \frac{a_{G*}}{a_G a_*} \tag{S.24}$$

$$K_{3,F} = \frac{a_F a_*}{a_{F*}} \tag{S.25}$$

$$K_{3,S} = \frac{a_S a_*}{a_{S*}} \tag{S.26}$$

$$K_4 = \frac{a_{W*}}{a_W a_*} \tag{S.27}$$

$$K_5 = \frac{a_{2W*}}{a_W a_{W*}} \tag{S.28}$$

In addition, the kinetically relevant bound glucose intermediates leading to fructose, $(R^*)_F$, or sorbose, $(R^*)_S$, formation are quasi-equilibrated with the respective hydride shift transition state as follows:

$$K_{R,F} = \frac{a_{\ddagger,F}}{a_{G*}} \tag{S.29}$$

$$K_{R,S} = \frac{a_{\ddagger,S}}{a_{G*}} \tag{S.30}$$

Eqs. (S.29) and (S.30) couple together the formation of the kinetically relevant bound glucose intermediate from the adsorbed glucose intermediate with the subsequent formation of the hydride shift transition state into a single equilibrium coefficient, $K_{R,i}$. Solving Eqs. (S.29) and (S.30) for $a_{\ddagger,F}$ and $a_{\ddagger,S}$, isomerization rates can then be expressed as:

$$r_{isom,F} = \frac{k_{2,F}}{\gamma_{\ddagger,F}} K_{R,F} a_{G*} (1 - \eta_F) \tag{S.31}$$

$$r_{isom,S} = \frac{k_{2,S}}{\gamma_{\ddagger,S}} K_{R,S} a_{G*} (1 - \eta_S) \tag{S.32}$$

And further expressed using Eq. (S.24) as:

$$r_{isom,F} = \frac{k_{2,F}}{\gamma_{\ddagger,F}} K_{R,F} K_1 a_G a_* (1 - \eta_F) \tag{S.33}$$

$$r_{isom,S} = \frac{k_{2,S}}{\gamma_{\ddagger,S}} K_{R,S} K_1 a_G a_* (1 - \eta_S) \tag{S.34}$$

Eqs. (S.33) and (S.34) can be rewritten in terms of activity coefficients (γ_i) and concentrations (c_i):

$$r_{isom,F} = \frac{k_{2,F}}{\gamma_{\ddagger,F}} K_{R,F} K_1 \gamma_G \gamma_* c_G c_* (1 - \eta_F) \quad \text{(S.35)}$$

$$r_{isom,S} = \frac{k_{2,S}}{\gamma_{\ddagger,S}} K_{R,S} K_1 \gamma_G \gamma_* c_G c_* (1 - \eta_S) \quad \text{(S.36)}$$

Total Lewis acid site concentrations ($c_{*,tot}$) are related to the concentrations of unoccupied sites (c_*) and sites with bound monosaccharide or solvent molecules from Scheme S.1 through the following site balance:

$$c_{*,tot} = c_* + c_{G*} + c_{R,F} + c_{R,S} + c_{F*} + c_{S*} + c_{W*} + c_{2W*} \quad \text{(S.37)}$$

Eq. (S.37) can be rewritten using Eqs. (S.24)-(S.30):

$$c_{*,tot} = c_* + \frac{K_1 a_G \gamma_* c_*}{\gamma_{G*}} + \frac{K_1 K_{R,F} a_G \gamma_* c_*}{\gamma_{R,F}} + \frac{K_1 K_{R,S} a_G \gamma_* c_*}{\gamma_{R,S}} + \frac{a_F \gamma_* c_*}{K_{3,F} \gamma_{F*}} + \frac{a_S \gamma_* c_*}{K_{3,S} \gamma_{S*}} + \frac{K_4 a_W \gamma_* c_*}{\gamma_{W*}} + \frac{K_4 K_5 a_W^2 \gamma_* c_*}{\gamma_{2W*}} \quad \text{(S.38)}$$

c_* can be factored out of the right-hand side of Eq. (S.38) leading to the following equation:

$$c_{*,tot} = c_* \left(1 + \frac{K_1 a_G \gamma_*}{\gamma_{G*}} + \frac{K_1 K_{R,F} a_G \gamma_*}{\gamma_{R,F}} + \frac{K_1 K_{R,S} a_G \gamma_*}{\gamma_{R,S}} + \frac{a_F \gamma_*}{K_{3,F} \gamma_{F*}} + \frac{a_S \gamma_*}{K_{3,S} \gamma_{S*}} + \frac{K_4 a_W \gamma_*}{\gamma_{W*}} + \frac{K_4 K_5 a_W^2 \gamma_*}{\gamma_{2W*}}\right) \quad \text{(S.39)}$$

Eq. (S.39) can then be rewritten in terms of fractional coverages (θ_i) of each bound adsorbate:

$$c_{*,tot} = c_* \left(\theta_* + \theta_{G*} + \theta_{R*,F} + \theta_{R*,S} + \theta_{F*} + \theta_{S*} + \theta_{W*} + \theta_{2W*}\right) \quad \text{(S.40)}$$

These fractional coverage terms are located in the isomerization rate expression denominator prior to establishing the most abundant surface intermediates.

From spectroscopic evidence discussed in the main text and both first-order and zero-order kinetic behavior in initial glucose activity, the most abundant surface intermediates are the Lewis acid site with two bound water molecules at dilute glucose concentrations (<1200 mol m^{-3}) and the Lewis acid site with adsorbed glucose at high glucose concentrations (>2700 mol m^{-3}). Eq. (S.39) can then be reduced to:

$$c_{*,tot} = c_* \left(\frac{K_1 a_G \gamma_*}{\gamma_{G*}} + \frac{K_4 K_5 a_W^2 \gamma_*}{\gamma_{2W*}}\right) \quad \text{(S.41)}$$

Substitution of Eq. (S.41) into Eqs. (S.35) and (S.36) and yields expressions for isomerization turnover rates per total Lewis acid site in terms of initial glucose thermodynamic activity:

$$\frac{\mathrm{r_{isom,F}}}{c_{*,tot}} = \frac{\frac{k_{2,F}}{\gamma_{\ddagger,\mathrm{F}}} K_{R,F} K_1 a_G (1-\eta_F)}{\left(\frac{K_4 K_5 a_W^2}{\gamma_{2W*}} + \frac{K_1 a_G}{\gamma_{G*}}\right)} \tag{S.42}$$

$$\frac{\mathrm{r_{isom,S}}}{c_{*,tot}} = \frac{\frac{k_{2,S}}{\gamma_{\ddagger,\mathrm{S}}} K_{R,S} K_1 a_G (1-\eta_S)}{\left(\frac{K_4 K_5 a_W^2}{\gamma_{2W*}} + \frac{K_1 a_G}{\gamma_{G*}}\right)} \tag{S.43}$$

This expression matches the rate equation labeled Eq. (8) in the main text and can be rearranged to follow a Langmuir Hinshelwood format which holds for either product:

$$r_i = \frac{\gamma_{G*}}{\gamma_{\ddagger,\mathrm{i}}} \frac{\frac{K_1 \gamma_{2W*}}{K_4 K_5 \gamma_{G*}} K_{R,i} k_{2,i} \frac{a_G}{a_W^2} (1-\eta_i)}{1 + \frac{K_1 \gamma_{2W*}}{K_4 K_5 \gamma_{G*}} \frac{a_G}{a_W^2}} \tag{S.44}$$

Apparent first-order and zero-order rate constants can then be defined as per the main text:

$$k_{app,first,i} = \frac{K_1 K_{R,F} k_{2,F} \gamma_{2W*}}{K_4 K_5 \gamma_{\ddagger,\mathrm{F}}} \tag{S.45}$$

$$k_{app,zero,i} = K_{R,i} k_{2,i} \frac{\gamma_{G*}}{\gamma_{\ddagger,\mathrm{i}}} \tag{S.46}$$

The equilibrium coefficient corresponding to the competitive adsorption of glucose and water is not dependent on the product formed and can be defined as:

$$K_{app,comp} = \frac{k_{app,first,i}}{k_{app,zero,i}} = \frac{K_1 \gamma_{2W*}}{K_4 K_5 \gamma_{G*}} \tag{S.47}$$

Eqs. (S.44) can then be rewritten using Eqs. (S.45)-(S.47) into:

$$r_i = \frac{k_{app,zero,i} K_{app,comp} \frac{a_G}{a_W^2} (1-\eta_i)}{1 + K_{app,comp} \frac{a_G}{a_W^2}} \tag{S.48}$$

Rate and equilibrium constants from Eqs. (S.24)-(S.30) reflect free energy differences between transition states, reactants, and solvent molecules:

$$K_1 = e^{\left(-\left(\Delta G_{G*}^0 - \Delta G_G^0 - \Delta G_*^0\right)/RT\right)} \tag{S.49}$$

$$K_{R,F} = e^{\left(-\left(\Delta G^0_{R,F} - \Delta G^0_{G*}\right)/RT\right)} \quad \text{(S.50)}$$

$$K_{R,S} = e^{\left(-\left(\Delta G^0_{R,S} - \Delta G^0_{G*}\right)/RT\right)} \quad \text{(S.51)}$$

$$k_{2,F} = \frac{k_B T}{h} e^{\left(-\left(\Delta G^0_{\ddagger,F} - \Delta G^0_{R,F}\right)/RT\right)} \quad \text{(S.52)}$$

$$k_{2,S} = \frac{k_B T}{h} e^{\left(-\left(\Delta G^0_{\ddagger,S} - \Delta G^0_{R,S}\right)/RT\right)} \quad \text{(S.53)}$$

$$K_4 = e^{\left(-\left(\Delta G^0_{W*} - \Delta G^0_{W} - \Delta G^0_{*}\right)/RT\right)} \quad \text{(S.54)}$$

$$K_5 = e^{\left(-\left(\Delta G^0_{2W*} - \Delta G^0_{W} - \Delta G^0_{W*}\right)/RT\right)} \quad \text{(S.55)}$$

Rewriting apparent first-order rate constants, $k_{app,first,F}$ and $k_{app,first,S}$, from Eqs. (S.45) and (S.46) in terms of free energies using Eqs. (S.49)-(S.55) gives the following expressions:

$$k_{app,first,F} = \frac{K_1 K_{R,F} k_{2,F} \gamma_{2W*}}{K_4 K_5 \gamma_{\ddagger,F}} = \frac{k_B T}{h} e^{\left(-\left(\left(\Delta G^0_{\ddagger,F} + 2\Delta G^0_{W}\right) - \left(\Delta G^0_{G} + \Delta G^0_{2W*}\right)\right)/RT\right)} \quad \text{(S.56)}$$

$$k_{app,first,S} = \frac{K_1 K_{R,S} k_{2,S} \gamma_{2W*}}{K_4 K_5 \gamma_{\ddagger,S}} = \frac{k_B T}{h} e^{\left(-\left(\left(\Delta G^0_{\ddagger,S} + 2\Delta G^0_{W}\right) - \left(\Delta G^0_{G} + \Delta G^0_{2W*}\right)\right)/RT\right)} \quad \text{(S.57)}$$

These apparent first-order rate constants depend on the free energy of the bound glucose isomerization transition state with two liquid phase solvent molecules relative to two bound water molecules with one liquid phase glucose molecule. Similarly, measured zero-order rate constants depend on the free energy of the hydride shift transition state relative to the adsorbed glucose intermediate:

$$k_{zero,F} = \frac{k_B T}{h} e^{\left(-\left(\Delta G^0_{\ddagger,F} - \Delta G^0_{G*}\right)/RT\right)} \quad \text{(S.58)}$$

$$k_{zero,S} = \frac{k_B T}{h} e^{\left(-\left(\Delta G^0_{\ddagger,S} - \Delta G^0_{G*}\right)/RT\right)} \quad \text{(S.59)}$$

Eqs. (S.56)-(S.59) therefore reflect the free energy differences reflected in first-order and zero-order rate constants quantified from initial rate measurements at low and high glucose activities.

S.5.2. Initial glucose isomerization rates and enthalpy and entropy determination

Figures S.35-S.37 show the raw data for sorbose formation rates on Ti-Beta-F-155 and both fructose and sorbose formation rates on Ti-Beta-OH-46 which forms the complete set of measured rates on Ti-Beta-F-155 and Ti-Beta-OH-46 when combined with the data presented in Figure 7 from the main text.

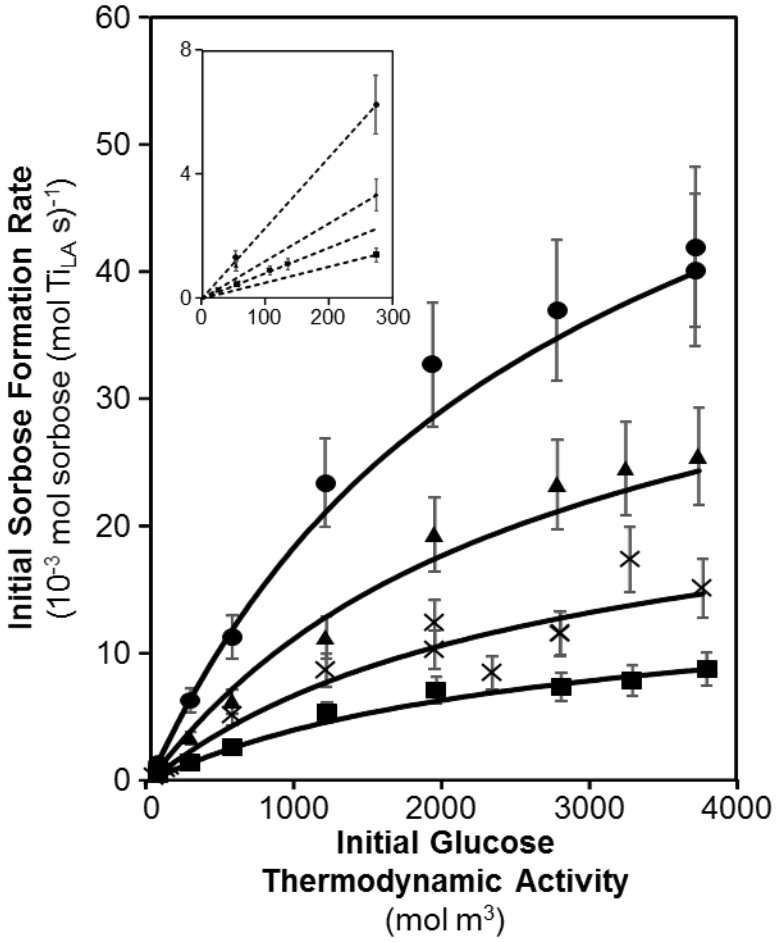

Figure S.35. Dependence of initial sorbose formation rates (pH 3) on Ti-Beta-F-155 on initial glucose thermodynamic activity (corresponding to 1-50 wt% initial glucose concentration) at 368 (■), 373 (X), 378 (▲), and 383 K (●). Solid lines for all data represent modeled regressions of the experimental data to the overall rate equation given in Eq. (16) in the main text using activation enthalpies and entropies given in Table 4.

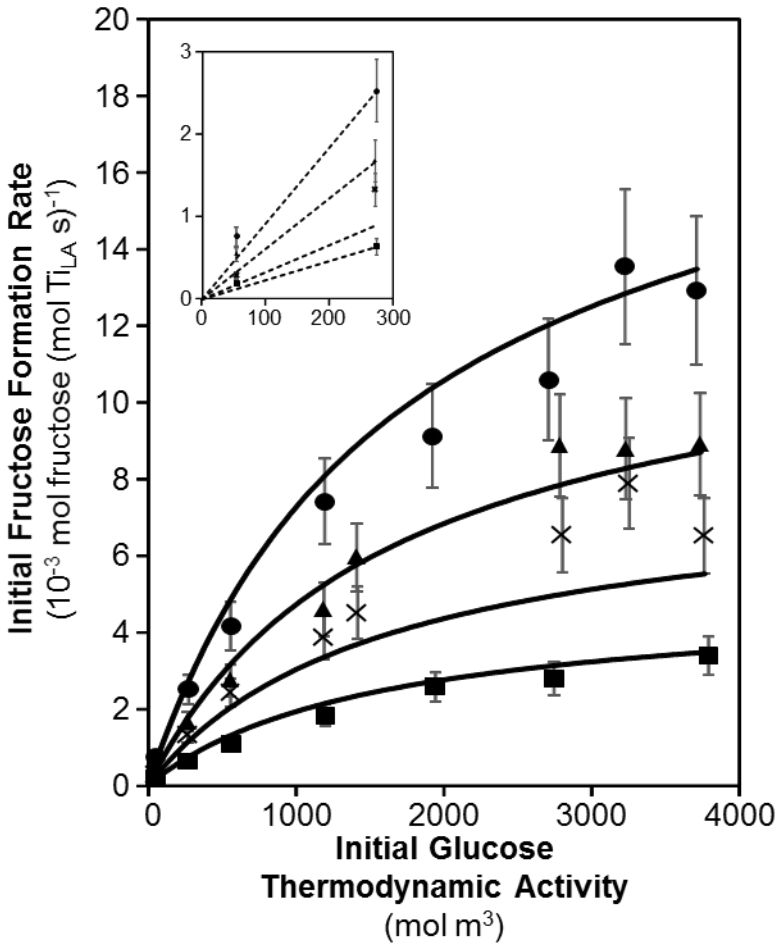

Figure S.36. Dependence of initial fructose formation rates (pH 3) on Ti-Beta-OH-46 on initial glucose thermodynamic activity (corresponding to 1-50 wt% initial glucose concentration) at 368 (■), 373 (X), 378 (▲), and 383 K (●). Solid lines for all data represent modeled regressions of the experimental data to the overall rate equation given in Eq. (16) in the main text using activation enthalpies and entropies given in Table 4.

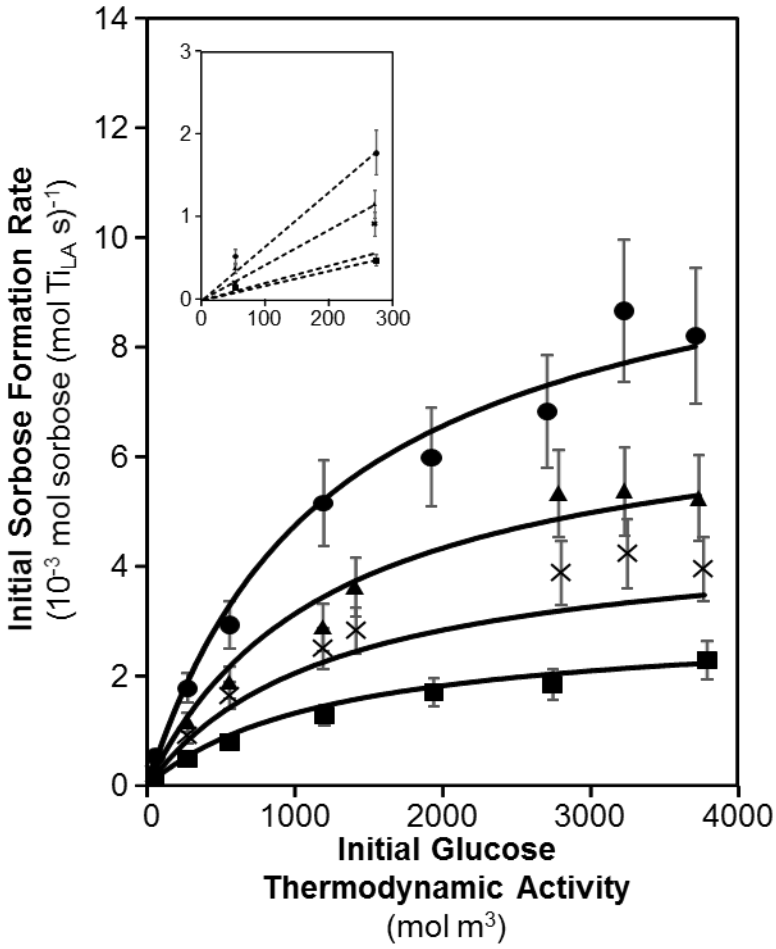

Figure S.37. Dependence of initial sorbose formation rates (pH 3) on Ti-Beta-OH-46 on initial glucose thermodynamic activity (corresponding to 1-50 wt% initial glucose concentration) at 368 (■), 373 (X), 378 (▲), and 383 K (●). Solid lines for all data represent modeled regressions of the experimental data to the overall rate equation given in Eq. (16) in the main text using activation enthalpies and entropies given in Table 4.

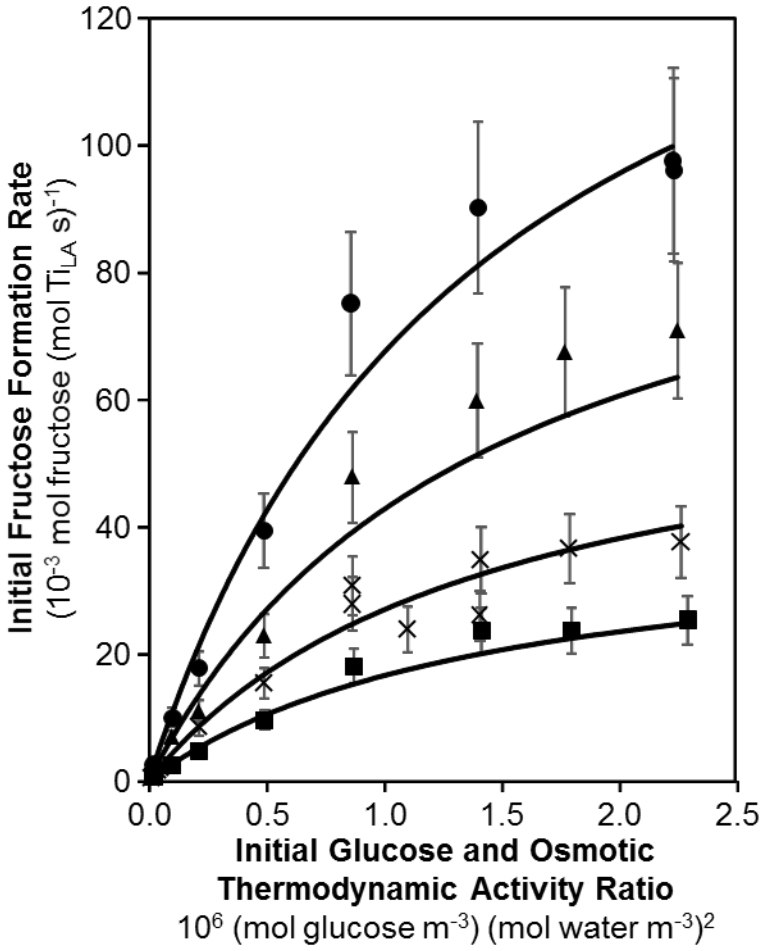

Figure S.38. Dependence of initial fructose formation rates (pH 3) on Ti-Beta-F-155 on initial glucose and osmotic thermodynamic activity ratio (corresponding to 1-50 wt% initial glucose concentration) at 368 (■), 373 (X), 378 (▲), and 383 K (●). Solid lines for all data represent modeled regressions of the experimental data to the overall rate equation given in Eq. (16) in the main text using activation enthalpies and entropies given in Table 4.

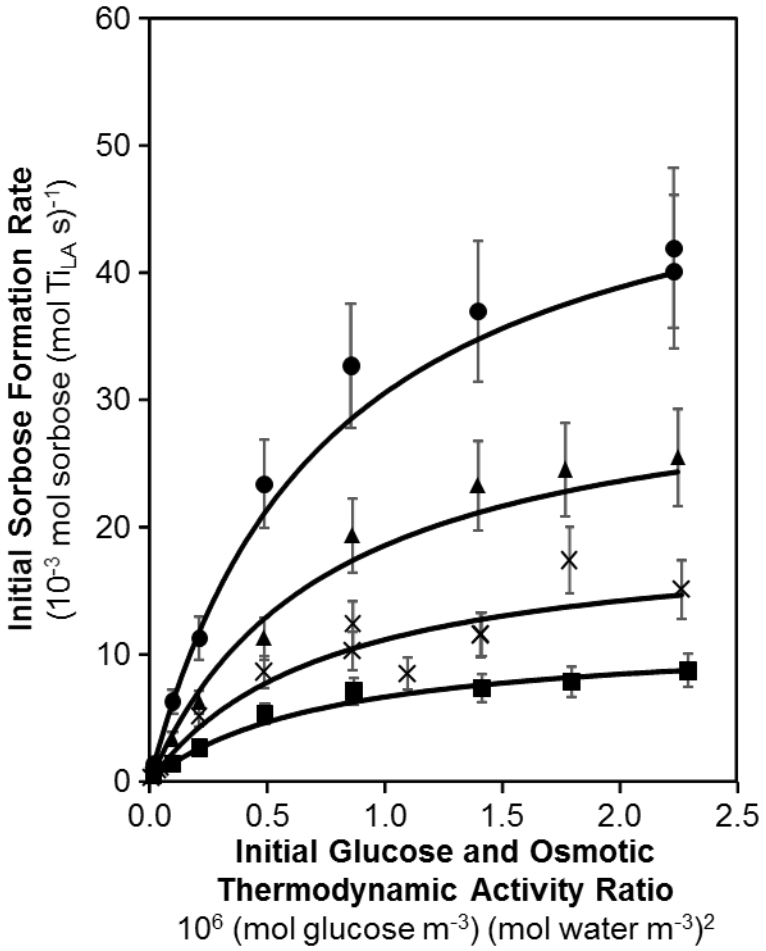

Figure S.39. Dependence of initial sorbose formation rates (pH 3) on Ti-Beta-F-155 on initial glucose and osmotic thermodynamic activity ratio (corresponding to 1-50 wt% initial glucose concentration) at 368 (■), 373 (X), 378 (▲), and 383 K (●). Solid lines for all data represent modeled regressions of the experimental data to the overall rate equation given in Eq. (16) in the main text using activation enthalpies and entropies given in Table 4.

S.5.3. Comparison of fitted thermodynamic properties with activity coefficient sets and for multiple fitting strategies

The modeled behavior derived from the regression of Eq. (16) in the main text to the experimental data set leads to the apparent enthalpy and entropy values reported in Table 4 when the experimental data points are weighted by experimental rate values. This weighting scheme minimizes the natural tendency for higher measured rates at increased glucose activities and temperature, and therefore higher absolute error differences between the experimental data and the model, to dominate the regression and instill systematic errors in the regressed parameters. Other weighting methods were investigated and did affect regressed activation enthalpies and entropies but led to systematic errors in model regression leading to exaggeration of rate measurements at higher glucose activities and temperatures. The presence of systemic errors derived from regressed parameters were studied by quantifying percent residuals using the following equation:

$$Percent\ Residual = \frac{(r_{exp} - r_{model})}{r_{exp}} * 100 \quad \text{(S.60)}$$

Figures S.38-S.41 show percent residuals as a function of glucose activity and temperature on both Ti-Beta-F-155 and Ti-Beta-OH-46 for both fructose and sorbose formation from rates given in Figures S.35-S.37 and Figure 7 in the main text. Systematic trends are not observed as a function of initial glucose activity, indicating that the model is not introducing systematic errors derived from the chosen fitting method. We note that negligible differences in fitted apparent enthalpies and entropies are observed when ideality is assumed for all solution-phase species ($\gamma_i \rightarrow 1$) and when activity coefficients are not adjusted for temperature changes. Glucose and water activities are therefore used throughout the main text.

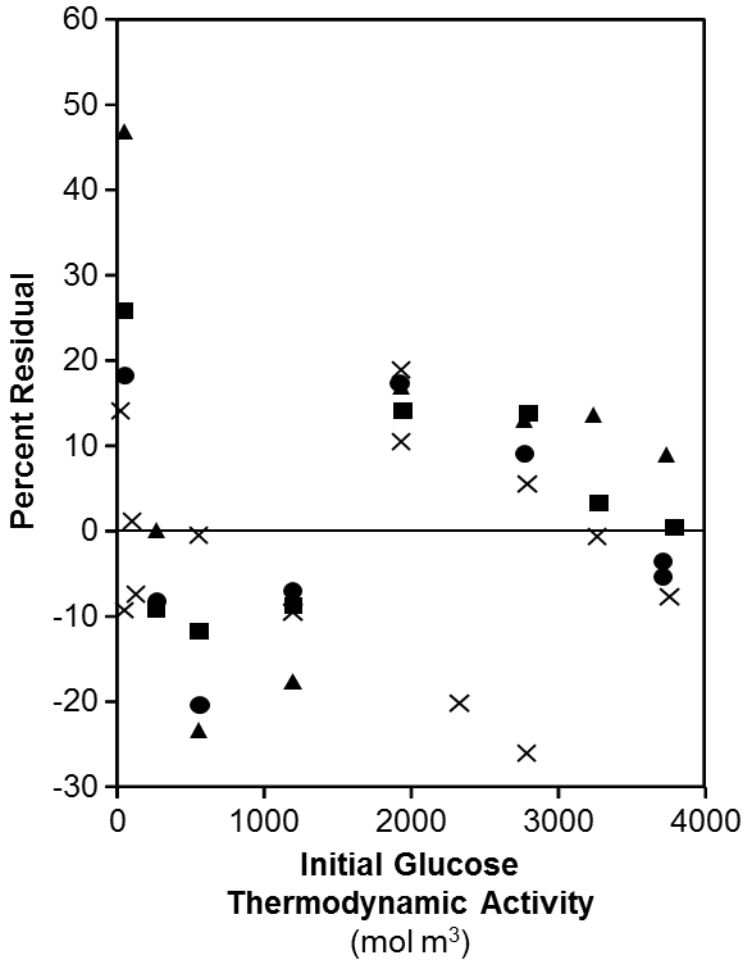

Figure S.40. Percent residual plot of fructose formation rates on Ti-Beta-F-155 as a function of initial glucose thermodynamic activity (corresponding to 1-50 wt% initial glucose concentration) at 368 (■), 373 (X), 378 (▲), and 383 K (●) comparing experimental rate measurements with modeled rate behavior from Eq. (16) from the main text. Percent residuals were obtained from Eq. (S.56).

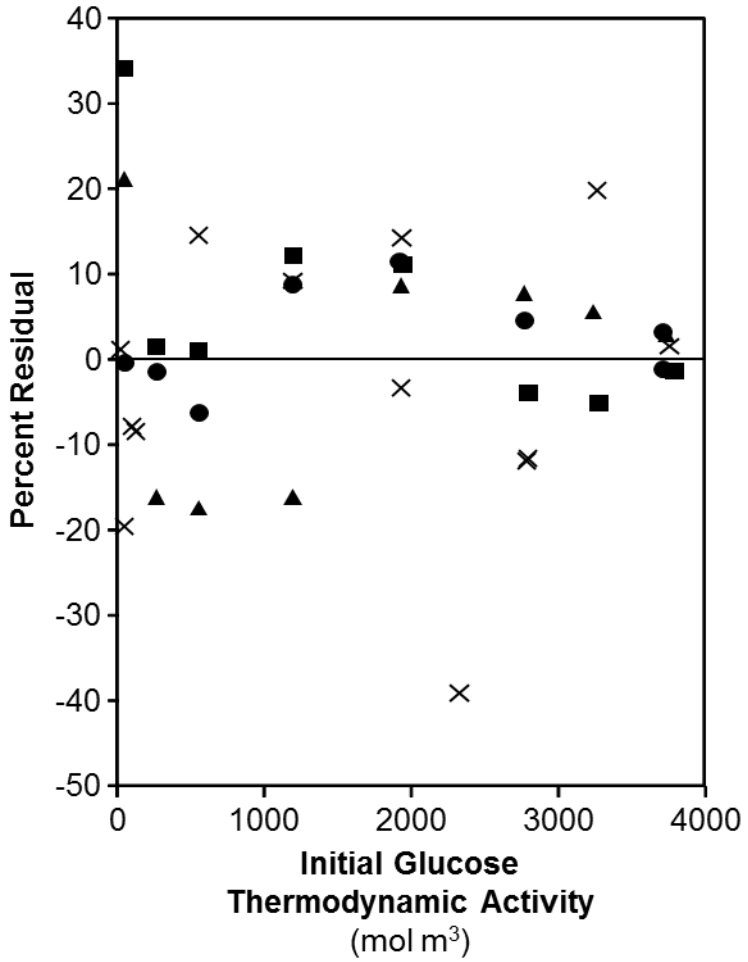

Figure S.41. Percent residual plot of sorbose formation rates on Ti-Beta-F-155 as a function of initial glucose thermodynamic activity (corresponding to 1-50 wt% initial glucose concentration) at 368 (■), 373 (X), 378 (▲), and 383 K (●) comparing experimental rate measurements with modeled rate behavior from Eq. (16) from the main text. Percent residuals were obtained from Eq. (S.56).

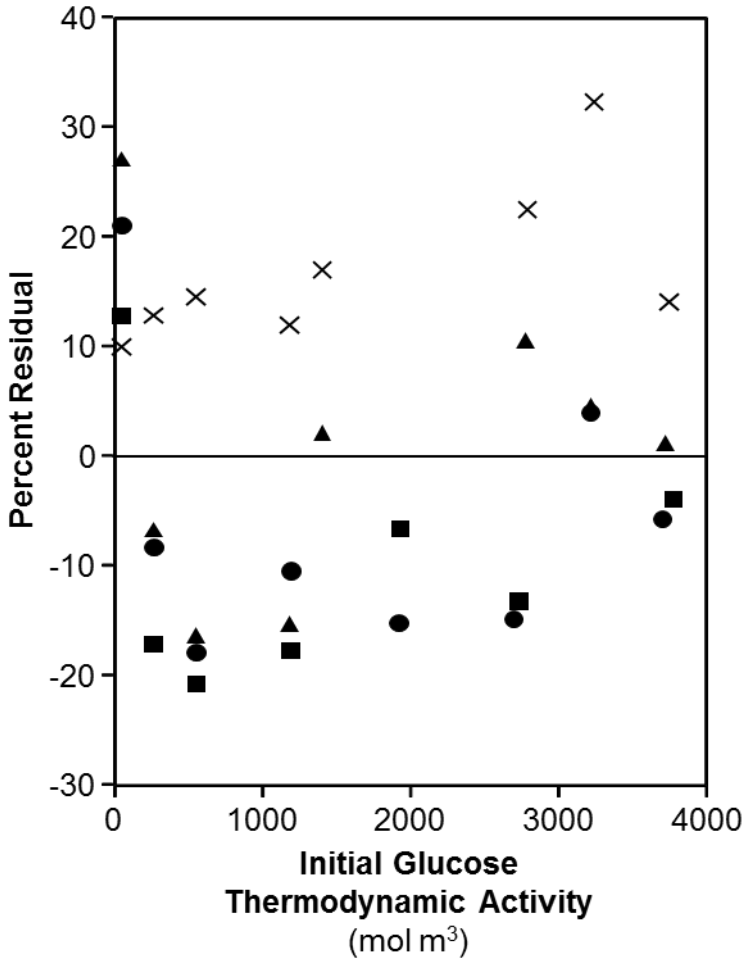

Figure S.42. Percent residual plot of fructose formation rates on Ti-Beta-OH-46 as a function of initial glucose thermodynamic activity (corresponding to 1-50 wt% initial glucose concentration) at 368 (■), 373 (X), 378 (▲), and 383 K (●) comparing experimental rate measurements with modeled rate behavior from Eq. (16) from the main text. Percent residuals were obtained from Eq. (S.56).

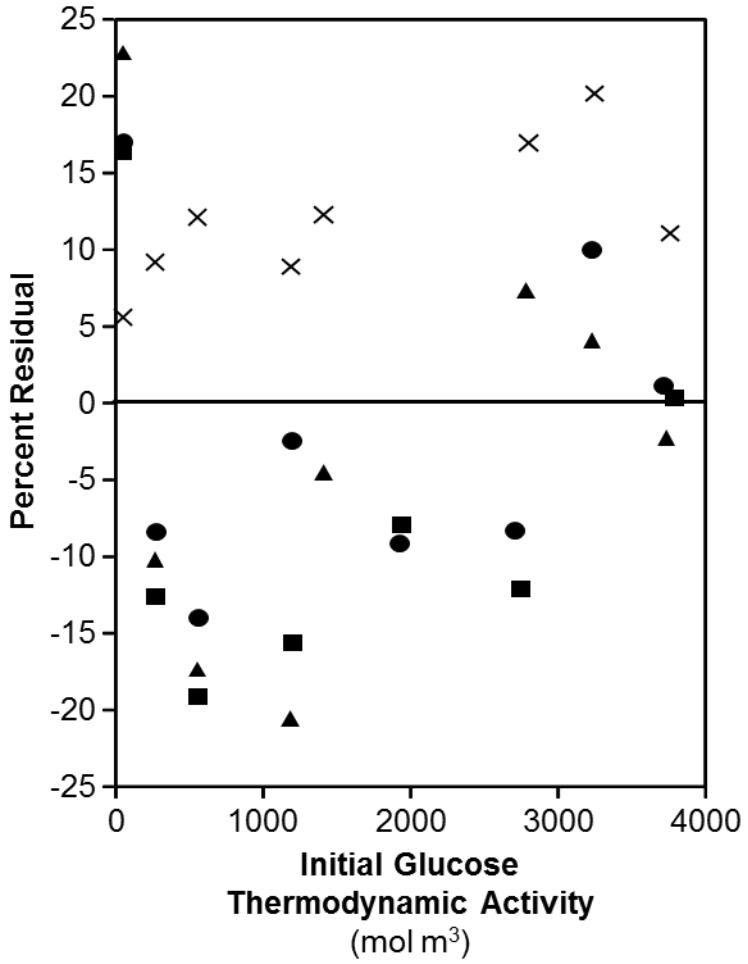

Figure S.43. Percent residual plot of sorbose formation rates on Ti-Beta-OH-46 as a function of initial glucose thermodynamic activity (corresponding to 1-50 wt% initial glucose concentration) at 368 (■), 373 (X), 378 (▲), and 383 K (●) comparing experimental rate measurements with modeled rate behavior from Eq. (16) from the main text. Percent residuals were obtained from Eq. (S.56).

The regressed rates derived from the apparent enthalpies and entropies listed in Table 4 of the main text predict zero-order rate constants that are higher than the rates measured at high glucose activities where Lewis acidic Ti sites are covered with bound glucose MARIs as seen from ATR-IR spectra. These differences result from measured isomerization rates that are not precisely zero-order at high glucose activities at all temperatures as shown in Figures S.43, but are less significant for measured first-order rate constants (Figure S.42). First-order and zero-order rate constants can then be estimated from single rate measurements at low (a_G = 275 mol m^{-3}) and high (a_G = 3500 mol m^{-3}) glucose activities, respectively. Apparent activation enthalpies and entropies listed in Table S.5 were determined from these measured rates at consistent glucose activities.

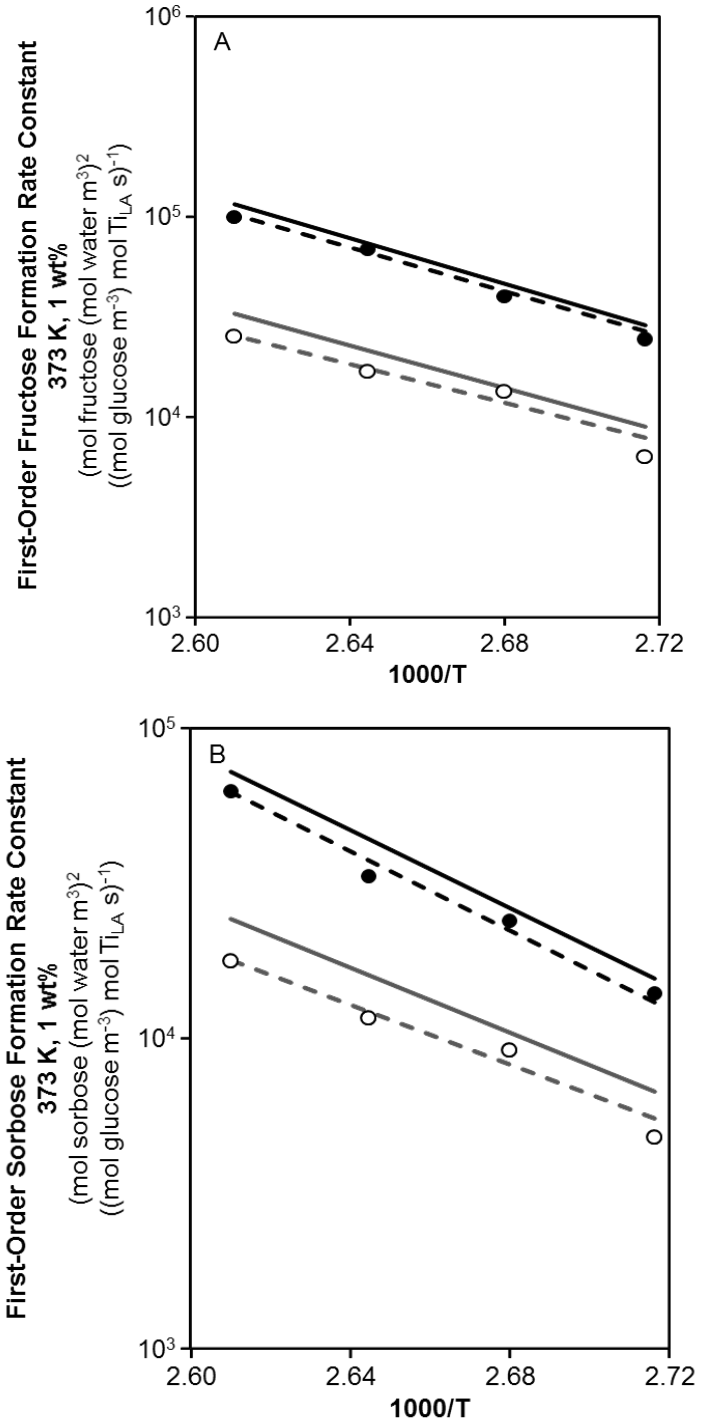

Figure S.44. Arrhenius plot for apparent first-order fructose (A) and sorbose (B) formation rate constants (368-383 K, 5 wt%) on Ti-Beta-F-155 (●) and Ti-Beta-OH-46 (○). Solid lines represent the results of the regression of Eq. (16) and dashed lines represent regressions using rate measurements at 5 wt% on Ti-Beta-F-155 (black) and Ti-Beta-OH-46 (gray). Both regression lines follow the Eyring equation with activation enthalpies and entropies given in Table 4 of the main text and Table S.5, respectively.

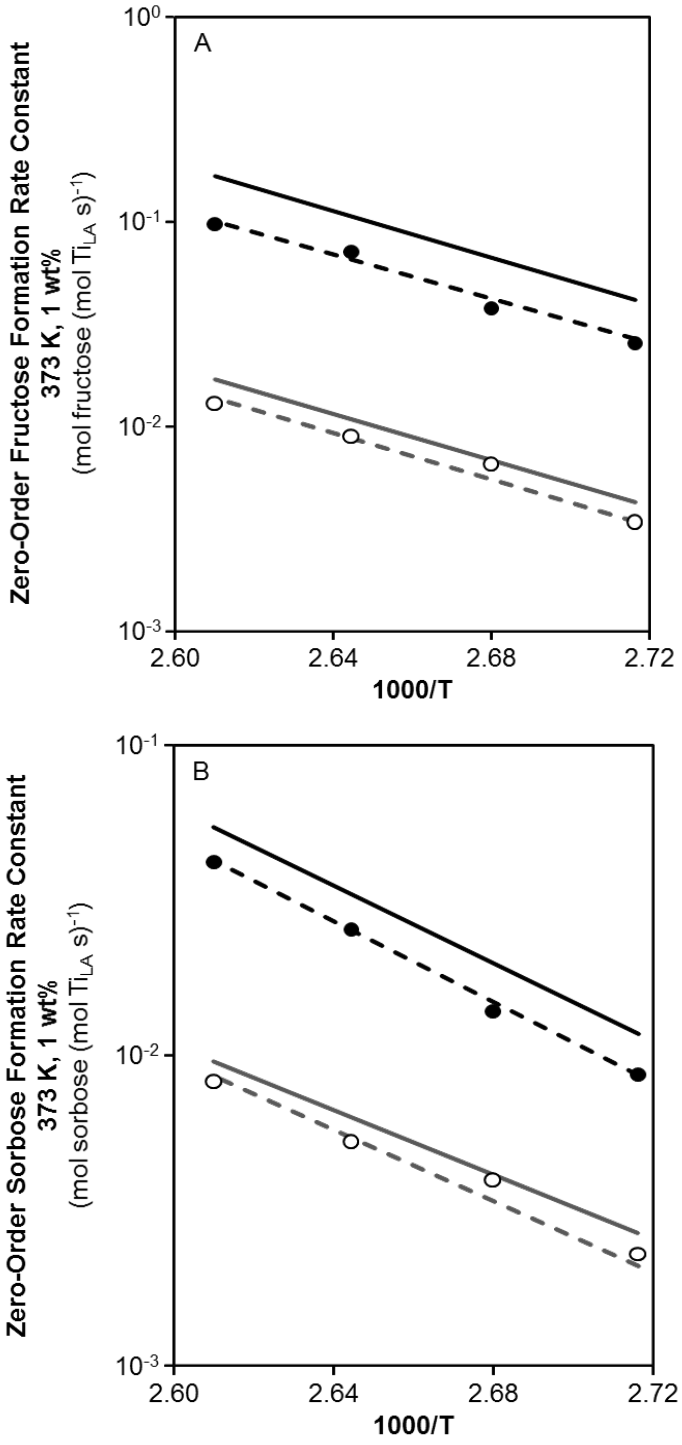

Figure S.45. Arrhenius plot for apparent zero-order fructose (A) and sorbose (B) formation rate constants (368-383 K, 50 wt%) on Ti-Beta-F-155 (●) and Ti-Beta-OH-46 (○). Solid lines represent the results of the regression of Eq. (16) and dashed lines represent regressions using rate measurements at 50 wt% on Ti-Beta-F-155 (black) and Ti-Beta-OH-46 (gray). Both regressions follow the Eyring equation with activation enthalpies and entropies given in Table 4 of the main text and Table S.5, respectively.

Table S.5. Apparent enthalpies and entropies for first- and zero-order rate constants describing fructose and sorbose formation on Ti-Beta-F-155 and Ti-Beta-OH-46 derived from single rate measurements at 5 and 50 wt% corresponding to first-order and zero-order rates. Differences in apparent activation enthalpies ($\Delta\Delta H_{app}$) and entropies ($\Delta\Delta S_{app}$) are listed as the difference between Ti-Beta-F-155 and Ti-Beta-OH-46.

Rate Constant	**ΔH_{app} (kJ mol^{-1})**		**ΔS_{app} (J mol^{-1} K^{-1})**		**$\Delta\Delta H_{app}$ (kJ mol^{-1})**	**$\Delta\Delta S_{app}$ (J mol^{-1} K^{-1})**
	Ti-Beta-F-155	**Ti-Beta-OH-46**	**Ti-Beta-F-155**	**Ti-Beta-OH-46**	**(F-OH)**	**(F-OH)**
$k_{zero,fructose}$	100	105	4	0	-5	4
$k_{first,fructose}$	102	89	124	78	13	46
$K_{comp,fructose}$	-2	16	-120	-78	18	42
$k_{zero,sorbose}$	122	106	53	0	16	53
$k_{first,sorbose}$	119	89	163	76	30	87
$K_{comp,sorbose}$	3	17	-90	-76	14	34

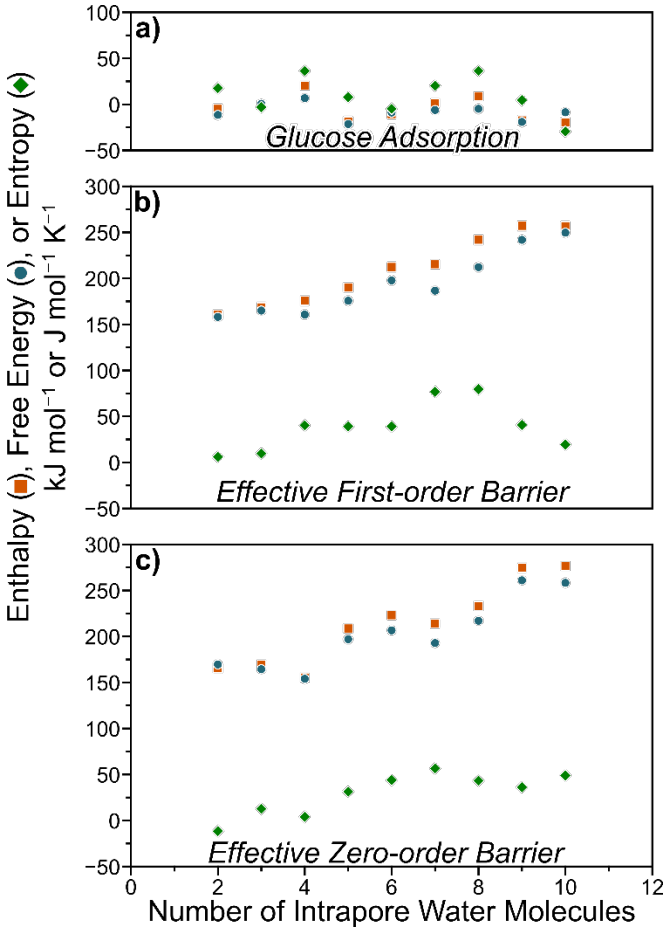

Figure S.46. DFT-calculated glucose adsorption energies (a) and effective first- (b) and zero-order (c) energy barriers for glucose-fructose isomerization. Enthalpies (■) and free energies (●) are shown in kJ mol^{-1} and entropies (◆) in J mol^{-1} K^{-1} (373 K). The intrapore water molecule density was assumed to remain constant during glucose adsorption and reaction for first-order analyses yet water molecules were allowed to reorient into lowest energy configurations in all cases.

References

1. Miyajima, K.; Sawada, M.; Nakagaki, M., Studiess on Aqueous Solutions of Saccharides. 1. Activity Coefficients of Monosaccharides in Aqueous Solutions at 25 Degrees C. *Bull. Chem. Soc. Jpn.* **1983,** *56* (6), 1620-1623.
2. Koretsky, M., *Engineering and Chemical Thermodynamics*. John Wiley & Sons, Inc.: New Jersey, 2004.
3. Baurecht, D.; Fringeli, U. P., Quantitative modulated excitation Fourier transform infrared spectroscopy. *Rev. Sci. Instrum.* **2001,** *72* (10), 3782.
4. Bregante, D. T.; Priyadarshini, P.; Flaherty, D. W., Kinetic and spectroscopic evidence for reaction pathways and intermediates for olefin epoxidation on Nb in *BEA. *J. Catal.* **2017,** *348*, 75-89.
5. Bermejo-Deval, R.; Assary, R. S.; Nikolla, E.; Moliner, M.; Roman-Leshkov, Y.; Hwang, S. J.; Palsdottir, A.; Silverman, D.; Lobo, R. F.; Curtiss, L. A.; Davis, M. E., Metalloenzyme-like catalyzed isomerizations of sugars by Lewis acid zeolites. *Proc. Natl. Acad. Sci. U. S. A.* **2012,** *109* (25), 9727-9732.
6. Vasko, P. D.; Blackwell, J.; Koenig, J. L., Infrared and Raman Spectroscopy of Carbohydrates. 1. Identification of O-H and C-H-Related Vibrational Modes for D-Glucose, Maltose, Cellobiose, and Dextran by Deuterium-Substitution Methods. *Carbohydr. Res.* **1971,** *19* (3), 297-+.
7. Vasko, P. D.; Blackwell, J.; Koenig, J. L., Infrared and Raman Spectroscopy of Carbohydrates. 2. Normal Coordinate Analysis of Alpha-D-Glucose. *Carbohydr. Res.* **1972,** *23* (3), 407-+.
8. Mathlouthi, M.; Luu, D. V., Laser-Raman Spectra of D-Glucose and Sucrose in Aqueous Solution. *Carbohydr. Res.* **1980,** *81* (2), 203-212.
9. Farges, F.; Brown, G. E.; Rehr, J. J., Coordination chemistry of Ti(IV) in silicate glasses and melts .1. XAFS study of titanium coordination in oxide model compounds. *Geochim. Cosmochim. Acta* **1996,** *60* (16), 3023-3038.
10. Gounder, R.; Davis, M. E., Monosaccharide and disaccharide isomerization over Lewis acid sites in hydrophobic and hydrophilic molecular sieves. *J. Catal.* **2013,** *308*, 176-188.
11. Roman-Leshkov, Y.; Moliner, M.; Labinger, J. A.; Davis, M. E., Mechanism of Glucose Isomerization Using a Solid Lewis Acid Catalyst in Water. *Angew. Chem.-Int. Edit.* **2010,** *49* (47), 8954-8957.